CFD Based Study of Unconventional Aeroengine Exhaust Systems

Tim D. Coates[*] and Gary J. Page[†]

Loughborough University, Loughborough, LE11 3TU, United Kingdom

The effect of upstream duct curvature on the exhaust plume of a jet engine is currently undocumented. Here, three different upstream curvatures are simulated using CFD to investigate the effect of upstream duct curvature on the over-expanded exhaust plume emanating from a rectangular nozzle of aspect ratio 5.8:1 at a nozzle pressure ratio of 2.5 and Reynolds number of 7.61×10^5. Due to the lack of available experimental data for curved ducts connected to high speed jets, the initial work was to validate the methodology for separate S-bend and rectangular nozzle high speed jet cases. These showed that RANS methods were poor for predicting secondary flows in the S-bend and for predicting mixing and potential core length in the rectangular jet. However, LES did show significant improvements for the rectangular jet and correctly predicts the shear layer mixing. Calculations were carried out using an unstructured, median-dual CFD solver with predominantly hexahedral elements containing approximately $65.5 - 67.5$ million nodes. For the combined S-bend and nozzle cases it was seen that increasing upstream duct curvature reduces the potential core length and increases losses in the upstream duct. Transverse total pressure gradients were also observed at the nozzle exit plane in both k-ϵ and WALE LES turbulence models, however to a significantly smaller degree in the latter. The upstream duct curvature was also seen to have an impact on the shock cell development, altering both number and location.

I. Introduction

A typical propulsive gas turbine installation uses a straight circular duct connecting to a circular nozzle. However, future civil and military applications may require a convoluted duct connecting to a non-circular nozzle. For example, the renewed interest in propfan or 'open rotor' engines, may necessitate a change in the location of the nozzle exits forcing the flow to be moved away from the centreline of the engine. Similarly, the low-observable nozzles on military aircraft are typically offset to prevent radar reflection from the core of the engine. Prior to this study, the research community has significantly contributed to the understanding of the flow through an S-bend duct for engine intakes, particularly in the formation of secondary flows. These secondary flows have a detrimental effect on an inlet application where a uniform flow is desired, whereas on an exhaust system this may be beneficial as the increase in swirl may enable more rapid jet shear layer mixing.

The formation of a secondary flow in an S-bend, as described by Miller[1] and Prandtl,[2] occurs due to a combination of adverse pressure gradients and centrifugal forces acting on the flow. At the start of the bend the flow is deflected to the outside of the duct as the pressure increases in the direction of the flow. This decelerates the boundary layer and in turn causes friction within the fluid further slowing the boundary layer. If the velocity decays sufficiently quickly then the flow separates from the wall and a secondary flow occurs. This secondary flow is a reverse flow formed as the low speed fluid moves around the walls towards the inside of the bend where there is a low static pressure region. This initialises the two vortices which can be seen in S-shaped ducts such as those encountered by Bansod and Bradshaw.[3]

The development of the flow in a square cross-sectioned, S-shaped duct was investigated by Ng et al.[4] and Taylor et al.[5] Flow separation was seen to occur along the lower wall of the first bend as well as along

---

[*]Ph.D. Student, Dept. of Aeronautical and Automotive Engineering. Email: t.coates@lboro.ac.uk, Tel: +44 (0) 1509 227282

[†]Senior Lecturer, Dept. of Aeronautical and Automotive Engineering, AIAA Senior Member. Email: g.j.page@lboro.ac.uk, Tel: +44 (0) 1509 227205

the outer wall of the second bend by both groups of authors. However the secondary flow caused by the first bend is weakened throughout in the second bend due to the opposing swirl created by the secondary flow along the outer wall. Further research has also been conducted by Vakili et al.,[6–9] Smith et al.[10, 11] and Guo and Seddon.[12, 13]

The examination of the flow through a rectangular nozzle has also been extensively studied. Sforza et al.,[14] Trentacoste and Sforza[15] and Sforza[16] initially investigated rectangular nozzles. Their experimental and theoretical studies divided the exhaust plume of an incompressible jet into three sections: the potential core, where the centreline velocity u_c is constant; and two decay regions. The first decay region, the characteristic decay, is a two-dimensional decay where $u_c^2 \propto x^{-n}$ and $n \approx 1$ whilst the second decay region, the axisymmetric decay, is akin to the decay to infinity of axisymmetric jets where $u_c \propto x^{-1}$.

According to the studies by Trentacoste and Sforza[15] the lengths of these three sections, as well as the value of n, are seen to be functions of the nozzle aspect ratio. However the experiments by Sfeir[17] dispute the relationship between the nozzle aspect ratio and the length of the first, two dimensional, decay region. Using aspect ratios of 10, 20, and 30 Sfeir also noted that the lengths of the three sections differed when studying the decay of velocity or temperature, since temperature decays faster.

Tsuchiya et al.[18] later confirmed the findings by Sfeir,[17] showing that the temperature and velocity decay rates differ from each other using turbulent free jets issuing from rectangular exits. Tsuchiya et al. studied the effects of small aspect ratios and various upstream geometries, namely a smooth contraction, orifice plate and 400mm duct and discovered that axis switching occurs in the various experiments. Mi et al.,[19, 20] Gutmark and Grinstein[21] and Miller et al.[22] have also studied the effects on the evolution of the jet plume for a variety of nozzles, (including rectangular nozzles).

The use of LES for flow predictions, especially those involving the prediction of noise, has increased in recent years. Typically studies using LES have been constrained to axi-symmetric nozzles, Mendez et al.,[23] however rectangular nozzles are beginning to be investigated as well, Nichols et al.[24] These studies have shown a very good agreement between the experimental data and the LES predictions.

Here we aim to investigate the effects of upstream duct convolution with a converging S-duct, on the jet plume emanating from a convergent-divergent high aspect ratio nozzle. Due to the limited experience of using RANS or LES in such a geometry two validation studies of separate S-bend and rectangular nozzle cases are presented in section III in order to assess the capabilities and limitations of the CFD methodology. The study of the three different curvature unconventional aeroengine exhaust systems (UAES) using RANS and LES approaches are then shown in section IV.

II.   Methodology

This study primarily uses the Rolls-Royce solver, Hydra.[25] Hydra is a density-based solver for compressible flows in unstructured grids which allows the code to simulate flows of complex geometries easily. However, this comes at the cost of computational time and accuracy when compared to block structured solvers. Although unstructured spatial discretisation typically limits the solution to second order accuracy Hydra has been improved to avoid excess dissipation of resolved eddies. Page and McGuirk[26] have validated the Hydra code on a variety of flow problems including complicated geometries in which the code performed well.

II.A.   Governing Equations

The Cartesian tensor form of the spatially filtered, Favre averaged Navier-Stokes equations is

$$\frac{\partial}{\partial t} \int_{\Gamma} Q dV + \int_{\partial \Gamma} F(Q) \cdot n dS + \int_{\partial \Gamma} G(Q) \cdot n dS = 0$$

where

$$Q = \begin{bmatrix} \bar{\rho} \\ \bar{\rho}\tilde{u} \\ \bar{\rho}\tilde{v} \\ \bar{\rho}\tilde{w} \\ \tilde{E} \end{bmatrix}, \; F(Q) = \begin{bmatrix} \bar{\rho}\tilde{U}_n \\ \bar{\rho}\tilde{U}_n\tilde{u} + \hat{n}_x\bar{p} \\ \bar{\rho}\tilde{U}_n\tilde{v} + \hat{n}_y\bar{p} \\ \bar{\rho}\tilde{U}_n\tilde{w} + \hat{n}_z\bar{p} \\ \tilde{(U)}_n(\tilde{E} + \bar{p}) \end{bmatrix}$$

American Institute of Aeronautics and Astronautics

and $G(Q)$ contains the conduction and viscous flux terms. The overbar and tilde represent the un-weighted and density weighted filters respectively whilst an implicit filter is used by the finite volume discretisation scheme.

II.B. Discretisation

The flux between the median-dual control volumes (generated from the original mixed element mesh) is integrated over the faces of the volumes. The flux on the face at the midpoint of the edge ij, connecting the two nodes i and j, is found using the second-order accurate scheme of Moinier[27] such that

$$F_{ij} = \frac{1}{2} \left[F(Q_i) + F(Q_j) - d_{ij} \right]$$

given the smoothing term

$$d_{ij} = |A_{ij}|\epsilon(L_j^{lp}(Q) - L_i^{lp}(Q))$$

where L^{lp} is the pseudo Laplacian, ϵ is a user defined constant and

$$|A_{ij}| = \frac{\partial F}{\partial Q}.$$

In LES the dissipation of resolved eddies must be avoided, consequently the smoothing term, d_{ij}, is kept low. Initially the smoothing term was set to $\epsilon = 0.15$ during the LES calculations.

The standard third-order accurate, three stage Runge Kutta algorithm is used for the Temporal discretisation for LES. The RANS simulations all use a multigrid acceleration method with a variable timestep dependent on the CFL number.

II.C. Turbulence and Sub-grid Scale Models

In the Hydra RANS simulations the standard k-ϵ turbulence model and the Menter[28, 29] shear stress transport adaption of the k-ω turbulence model are used. The Wall-adapting local eddy-viscosity (WALE) sub-grid scale model,[30] equation 1, is used in the Hydra LES implementation.

$$\mu_{\mathrm{SGS}} = \rho \left(C_w l \right)^2 \frac{(\mathscr{S}_{ij}^d \mathscr{S}_{ij}^d)^{\frac{3}{2}}}{(\overline{S}_{ij}\overline{S}_{ij})^{\frac{5}{2}} + (\mathscr{S}_{ij}^d \mathscr{S}_{ij}^d)^{\frac{5}{4}}} \tag{1}$$

Such that the length scale, l, is defined as the cuberoot of the volume with the strain rate given by

$$\overline{S}_{ij} = \frac{1}{2} \left(\frac{\partial \overline{u}_i}{\partial x_j} + \frac{\partial \overline{u}_j}{\partial x_i} \right)$$

and the traceless symmetric part of the square of the velocity gradient tensor defined as

$$\mathscr{S}_{ij}^d = \frac{1}{2} \left(\overline{g}_{ij}^2 + \overline{g}_{ji}^2 \right) - \frac{1}{3}\delta_{ij}\overline{g}_{kk}^2$$

where $\overline{g}_{ij}^2 = \overline{g}_{ik}\overline{g}_{kj}$ is the square of the velocity gradient and δ_{ij} is the Kronecker delta. The WALE SGS model accomodates the effects of the rotational rate as well as the strain rate of a turbulent structure whilst the the Smagorinsky SGS model only relates the strain rate of the turbulent structure to the invariant. The near wall shear layer also tends to zero at the wall in the WALE SGS model unlike the Smagorinsky SGS model where it is kept at order $O(1)$.

II.D. Parallel Processing

The Hydra solver uses the MPI and OPlus libraries for parallel communication and the grid is partitioned at run time using ParMetis. Typically a 65×10^6 node mesh is run across 288 cores (24 nodes of 12 processors connected by Infiniband network) for around 48 hours to achieve $100,000$ timesteps. The LES cases were run for $100,000$ timesteps before the mean was turned on and then the mean was measured across the next $300,000$ timesteps.

American Institute of Aeronautics and Astronautics

III. Validation Study

Due to the lack of available experimental data an initial validation study was undertaken to assess the viability of the hydra code for both S-bend flows and turbulent jet flows. These two studies are briefly outlined below.

III.A. S-bend flows

The experiments of Ng et al.[4] were used as the basis for assessing the viability of the Hydra code for S-bend ducts. From the experimental data, test section 3 was chosen for the study as it had the greatest offset of the three cases at $1.3D_h$. The Reynolds number based on hydraulic diameter and inlet velocity is 1.47×10^5. Using a 9.2 million node, hexahedral mesh built in ICEM CFD (seen in figure 1), several simulations were conducted using the Hydra k-ϵ and k-ω SST turbulence models as well as with the ANSYS Fluent Reynolds-stress model. The experimental geometry both upstream and downstream of the test section were modelled in addition to the actual test section. The upstream section (shown in blue) was recreated in order to capture the influence of the contraction section on the inlet conditions whilst the down stream section (shown in purple) was modelled in order to view the behaviour of the secondary flows after the test section.

(a) Overall mesh, $901 \times 101 \times 101$ nodes

(b) S-bend region of Mesh, $401 \times 101 \times 101$ nodes
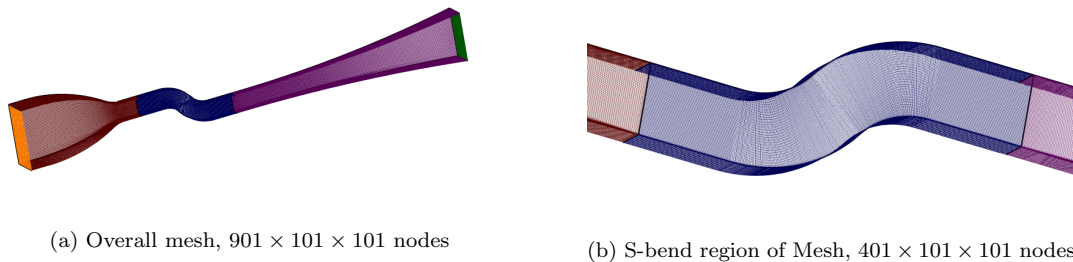
Figure 1: The mesh of the Ng 53.1° S-bend test section.

An overview of the flow through the S-bend using the k-ω turbulence model can be seen in figure 2. This clearly shows a region of separation occurring in the duct due to twin counter-rotating vortices created by the curvature of the duct. Figure 3 plots the static pressure coefficient along the centreline of the top and bottom duct walls and, as expected, a change of sign occurs in the static pressure coefficient along both walls. However the simulated static pressure recovery is significantly less than seen in the experiment and the point of inflection located on the bottom wall of the experiment at $s/D_h = 0.9$–1.3 is both weaker in the CFD predictions and later than expected.

(a) x-z plane along the centreline, $y = 0$
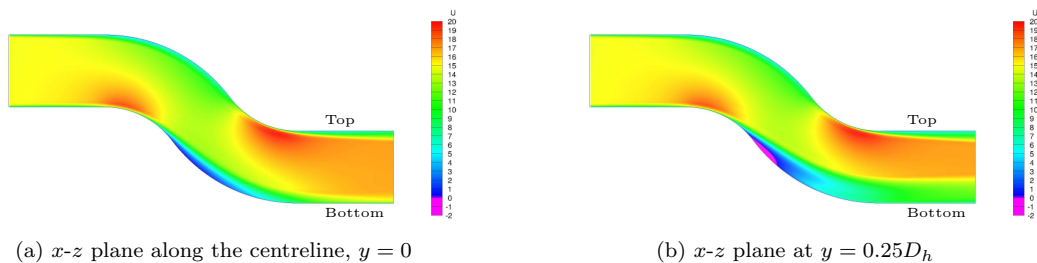
(b) x-z plane at $y = 0.25D_h$

Figure 2: An overview of axial velocity in the S-bend.

The exit plane of the test section showing total pressure coefficient contours can be seen in figure 4. The total pressure coefficient is defined as

$$C_p = \frac{p - p_s}{\frac{1}{2}\rho u_m^2}$$

where p_s is taken in the centre of the bottom floor in the initial straight section of the test duct and u_m is the mean inlet velocity. All three turbulence models show two distinct low pressure regions on the left side of the subfigures, caused by the stream wise vortices. However, in the experimental data these low-pressure
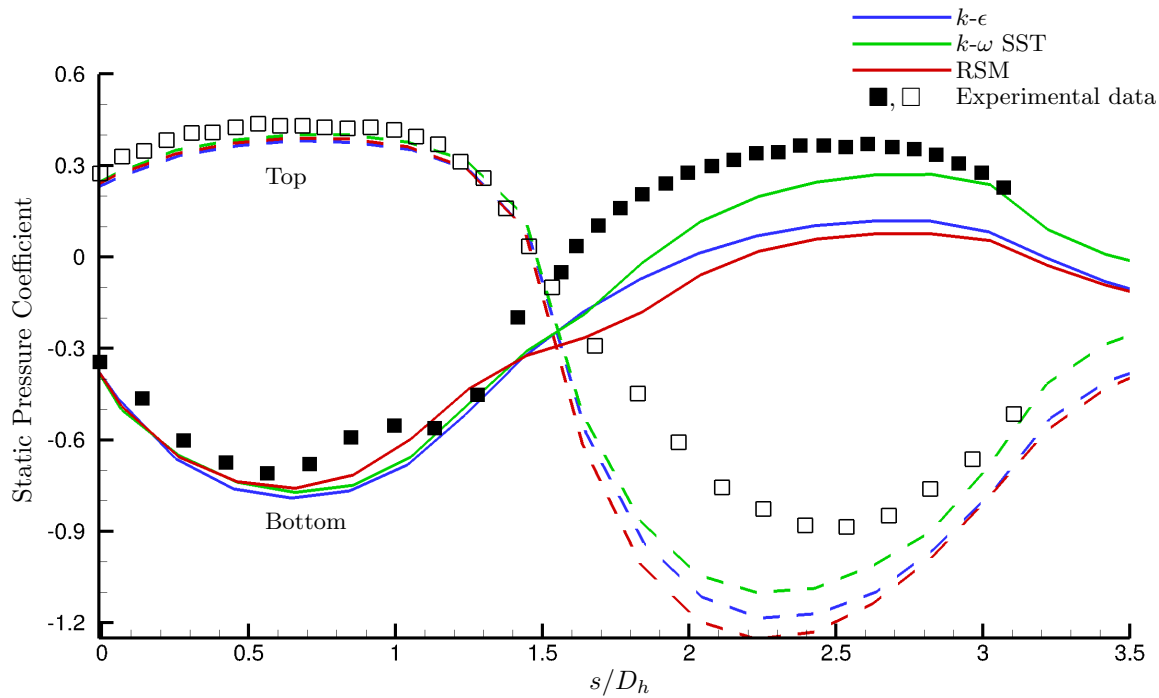
Figure 3: The Centreline static pressure distribution. The upper surface is denoted by the dashed line, the lower surface by the solid line.

regions appear to have merged into a single layer which is not reproduced by the simulations. In fact the simulated results match more closely to those of test section 2 in the experiments of Ng et al.[4] where the offset is only $1D_h$.

Figure 5 shows the cross-flow vectors of the simulations compared to experimental data. Here we see that an extra vortex, circulating in the opposite direction occurs in both the k-ϵ and k-ω models. Although not seen in test section 3, these additional vortices are present in test section 2 again suggesting that the strength of the secondary flow is being under predicted. Although the Reynolds-stress model does only show two vortices the vortex occurring closer to the sidewall is actually rotating in the opposite direction to that seen in the experiment.

Overall it appears that the k-ω model is the best approximation of the three turbulence models; however it still significantly under predicts the secondary flow. Consequently it is likely that a more expensive approach such as LES or DES will be required to achieve accurate predictions of secondary flows as demonstrated by Vuillerme et al.[31]

American Institute of Aeronautics and Astronautics

(a) Experimental data

(b) k-ϵ turbulence model

(c) k-ω SST turbulence model

(d) Reynolds-stress turbulence model
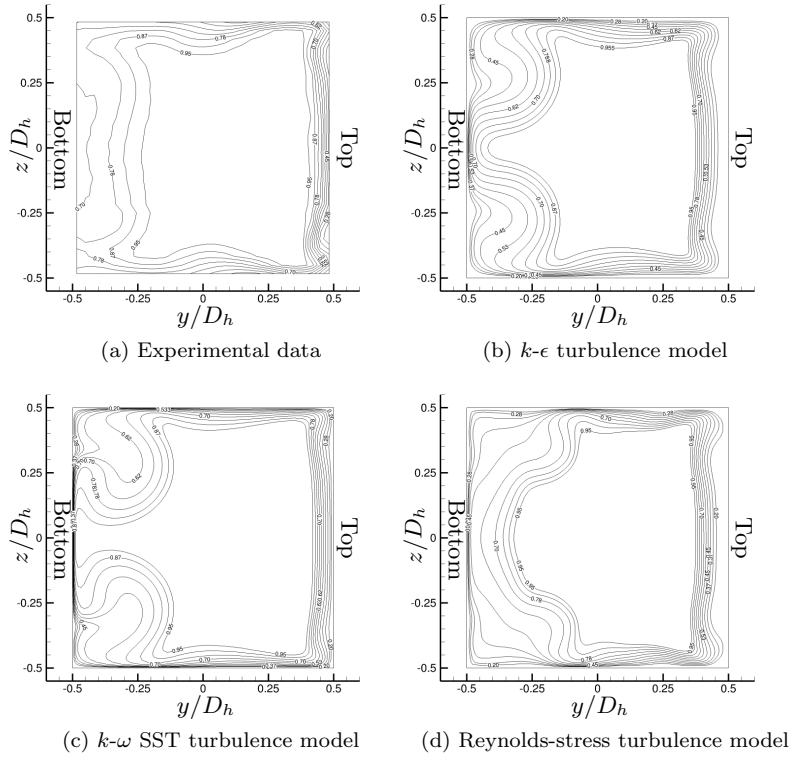
Figure 4: Total pressure contours at the test section outlet.

(a) Experimental data

(b) k-ϵ turbulence model

(c) k-ω SST turbulence model

(d) Reynolds-stress turbulence model
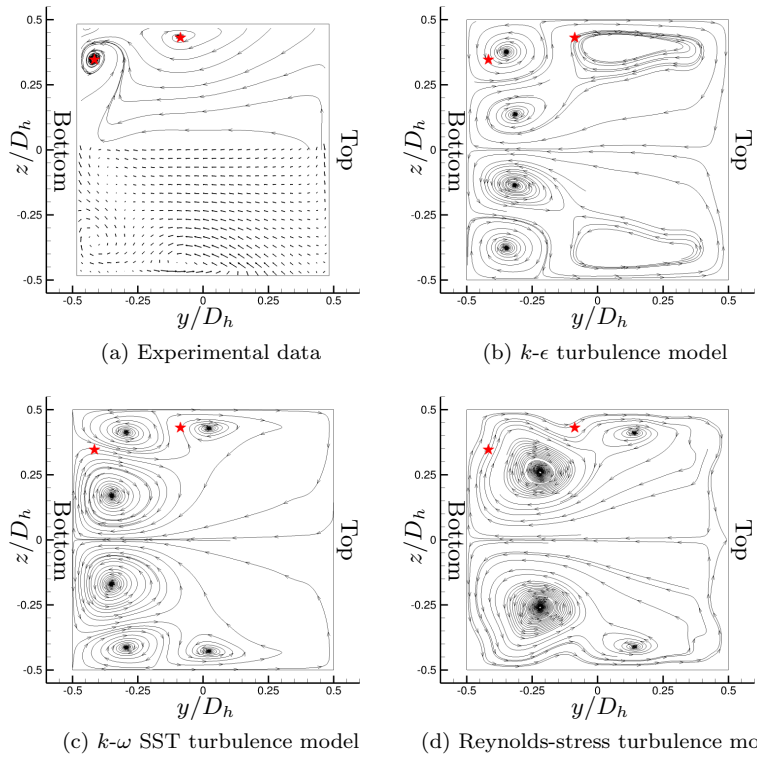
Figure 5: Crossflow velocity at the test section outlet. The red stars in figures 5b–5d denote the centre of the vortices seen in the experimental data.

III.B. Rectangular Nozzle

The experimental work of Behrouzi and McGuirk[32,33] was used in order to validate the Hydra code and assess its limitations with respect to the jet from a high aspect ratio nozzle. The simulations of the RRLU-1 rectangular nozzle were performed at a nozzle pressure ratio (NPR) of 2.5 at the inlet which gives a Reynolds number of 7.61×10^5 based on the hydraulic diameter and the fully expanded jet velocity at the nozzle exit. The experiments used an LDA system to measure the velocity and pitot probes for the pressure. Schlieren images were also taken of the flow using a rainbow filter to provide a contrast between compression and expansion waves.

III.B.1. Configuration

A picture of the experimental setup used in the RRLU1 experimental work of Behrouzi and McGuirk is shown in figure 6a with an overview of the mesh used in the validation study given in figure 6b. The geometry and unstructured hexahedral mesh were created using ICEM CFD. The mesh contains approximately 65 million nodes and has a y^+ value of about 1.2 at the nozzle exit. The specific details of the geometry and mesh are given later in section IV.A and section IV.B respectively.

The boundary conditions for the nozzle inlet were drawn from the experiments of Behrouzi and McGuirk. The pressure was set to $2.5P_s$ with $k = 84.4$ and $\epsilon = 2.17 \times 10^6$. The pressure of the coflow was 5pa above P_s in order to force the direction of the coflow downstream and prevent negative flow regions. The kinetic turbulent energy and dissipation rate were given by $k = 1.5$ and $\epsilon = 3,850$ respectively. The outlet was given the static pressure $P_s = 101,325$.

For the LES calculation the timestep was set to 0.114×10^6 and a value of between 0.25 and 0.35 was used for the WALE constant. The timestep is equivalent to 0.001816 non-dimensional time units. The mean flow was averaged across $30,000$ samples with each sample taken 10 timesteps apart. The mean is therefore taken across 2.25 complete passes throughout the domain at fully expanded jet velocity. Whilst this gives a good convergence near the nozzle more samples will need to be taken in order to accurately model the mean further downstream.
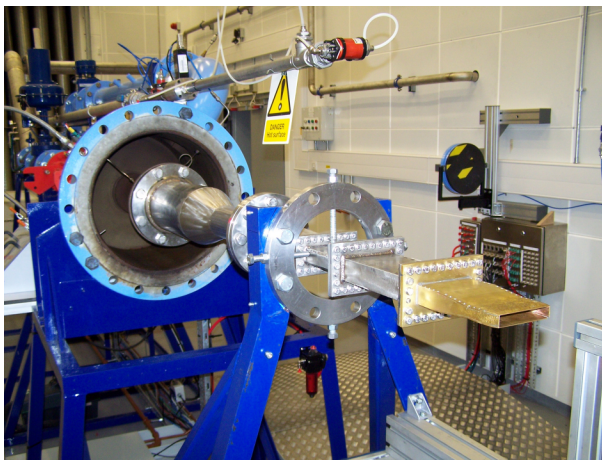
(a) Experimental setup
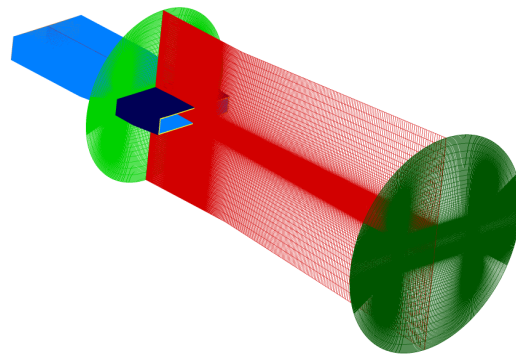
(b) Mesh Overview

Figure 6: Overview of the experimental setup and mesh used.

III.B.2. Results

Figure 8 shows the comparison of axial velocity across the minor axis plane of the duct between the LDA experimental data, RANS k-ϵ simulation and the LES WALE model. The potential core of the RANS simulation, figure 8b, is significantly longer than that of the experiment whilst the LES potential core length is shorter and matches more closely. This over-prediction of the potential core length is expected with the use of the k-ϵ turbulence model and is similarly shown in the following centreline plot, figure 7. In this figure the WALE SGS model appears to slightly shift the shock cell locations however it has a significantly better potential core decay, matching very closely with the LDA data. Several axial planes are seen in figure 9 showing the axial velocity. The high aspect ratio of the nozzle can easily be seen in the flow visualisations here. In figure 9a we can see that the final plane, $x/D_h = 15$, is a different shape to the same plane in figure 9b emphasising the effect of the overprediction of the potential core in the k-ϵ case.

The two CFD simulations pictured in figure 8 clearly show evidence of shock cells which are not obvious in the visualisation of the LDA measurements. Behrouzi and McGuirk used schlieren images of the flow, taken using a rainbow filter, to establish the presence and location of these shock cells. In figure 10 we have used the axial density gradient of the simulations to compare the shock cells with the schlieren image across the minor axis plane. The overall jet structure of the experiment is matched by the two simulations and both show the presence of shock cells. The k-ϵ case appears to include more shock cells than seen in the experiment which is consistent with the longer potential core length.

Figure 11 and figure 12 compare the axial velocity at several axial locations across the major and minor axis respectively. In each location, both in the major and minor axes, the LES significantly out performs the RANS simulation, matching both the centreline velocity and the gradient in the shear layer. The RANS simulation tends to over predict the centreline velocity and consequently has a steeper gradient in the shear layer. It should also be noted that the double peak in the velocity profile at the first axial station, $x/D_h = 1$, is due to the location of the shock cell relative to the axial station.

An instantaneous visualisation of Mach 0.5 is shown in figure 13. We can see that small scale fluctuations are generated at the nozzle lip and these is no laminar like initial shear layer. Together with the μ-SGS ratio visualisation seen in figure 14 the eddies appear to be reasonably well resolved near the nozzle exit. They are less well resolved further down stream, however this is less important in the flow as by this time the majority of the potential core as been mixed out.

Figure 14 shows the ratio of the mean sub-grid scale viscosity to kinematic viscosity. If this ratio is high, then significant stress is being carried by the sub-grid scale model and so the solution is a poorly resolved LES, conversely where the ratio is low the solution is well resolved. The plot clearly shows the importance of grid resolution and how sub-grid scale viscosity scales with l^2. The fine mesh region aligned with the nozzle lip is well resolved, but the expansion of the grid away from this coupled with significant unsteadiness gives a high mean sub-grid scale viscosity. This shows that highly clustered grids tailored to resolve mean gradients typically used in RANS calculations are poor for LES and small grid spacing needs to be maintained in all regions where unsteadiness is expected.
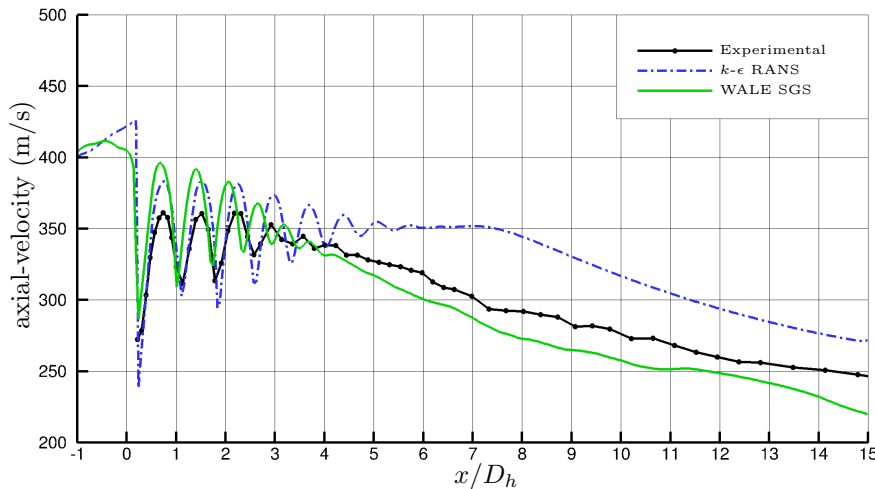

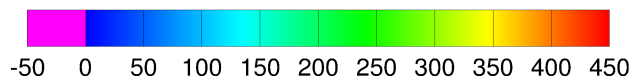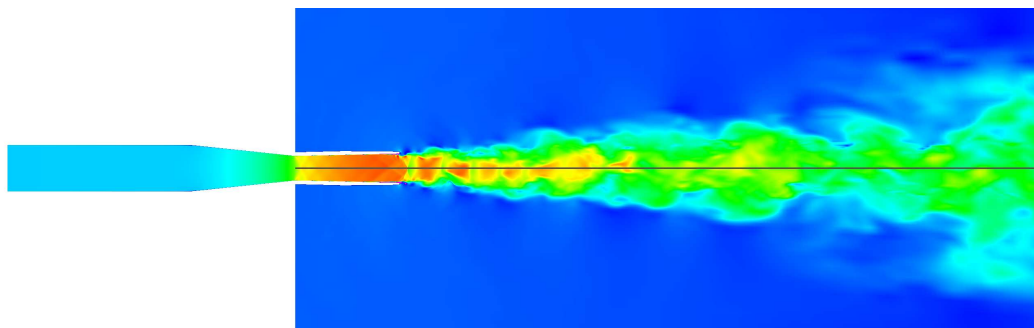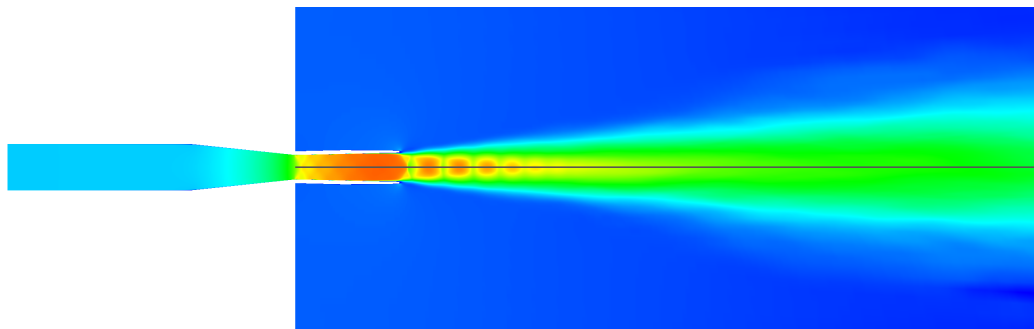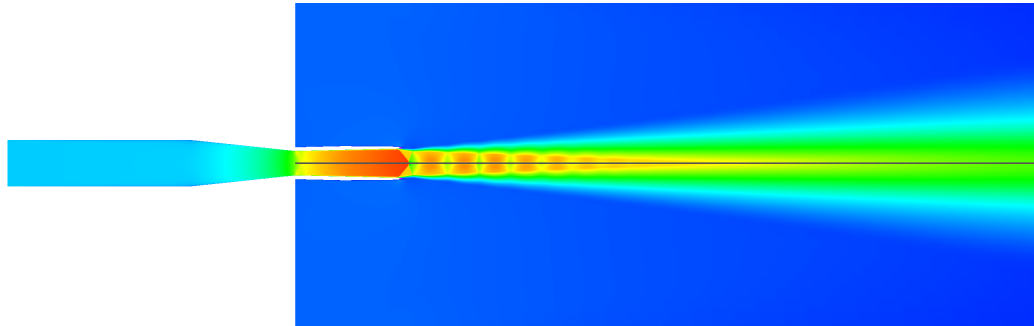Figure 7: Centreline comparison of axial velocity.

American Institute of Aeronautics and Astronautics

(a) Experimental LDA data

(b) k-ϵ RANS

(c) WALE LES mean

(d) WALE LES instantaneous
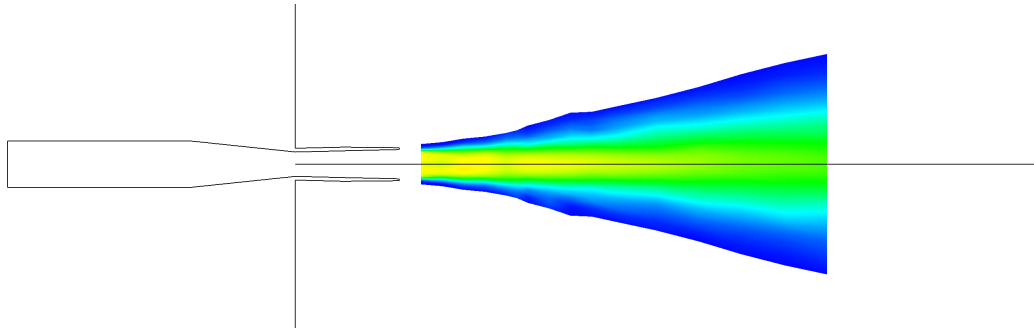

-50   0   50   100 150 200 250 300 350 400 450

Figure 8: Flow visualisation of axial velocity across the minor axis plane.

American Institute of Aeronautics and Astronautics
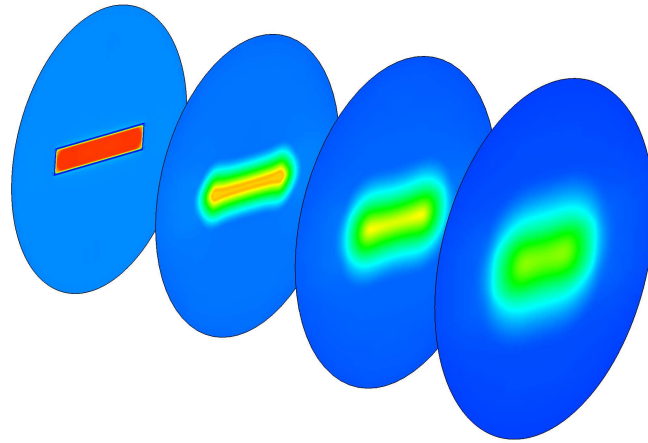
(a) k-ϵ RANS
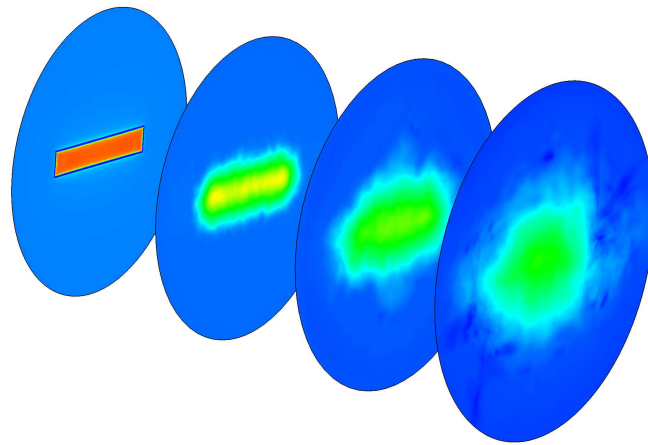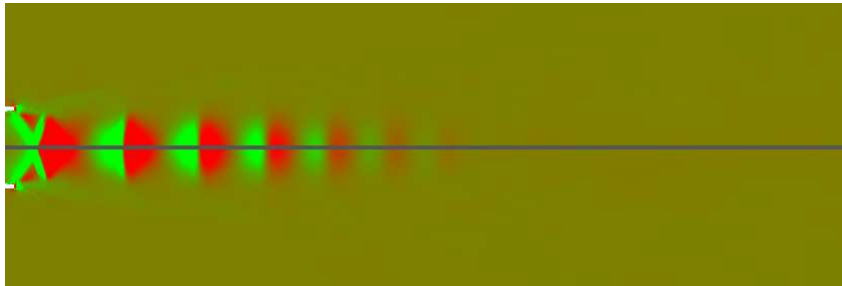

(b) WALE LES mean

(c) WALE LES instantaneous

-50   0   50   100 150 200 250 300 350 400 450
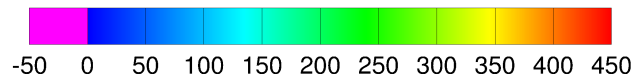
Figure 9: Flow visualisation of axial velocity at the nozzle exit, $5D_h$, $10D_h$ and $15D_h$ downstream.
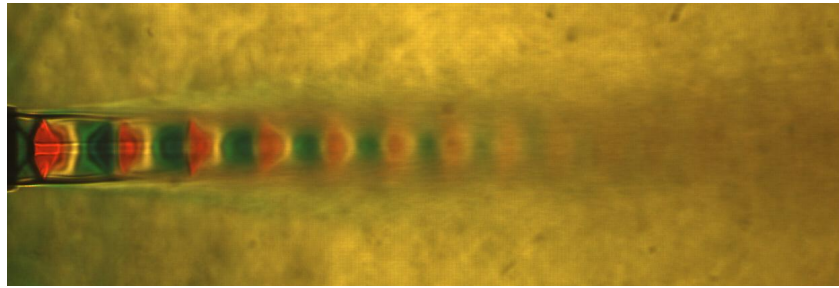
(a) Experiment schlieren image

(b) k-ϵ RANS
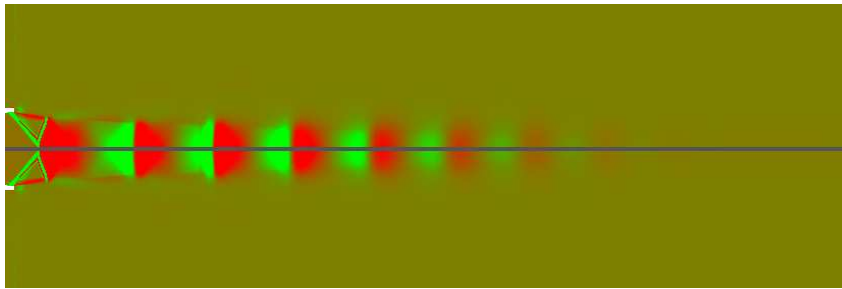
(c) WALE LES mean
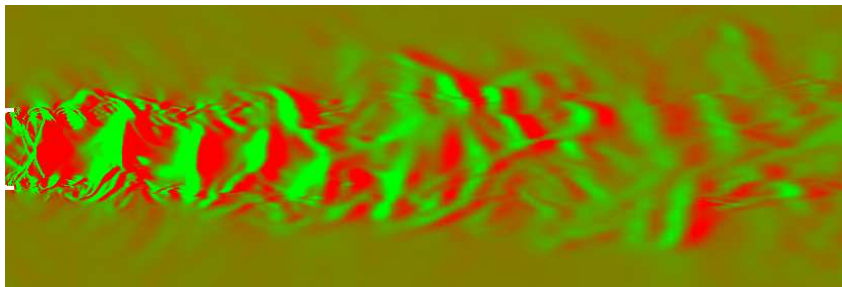
(d) WALE LES instantaneous

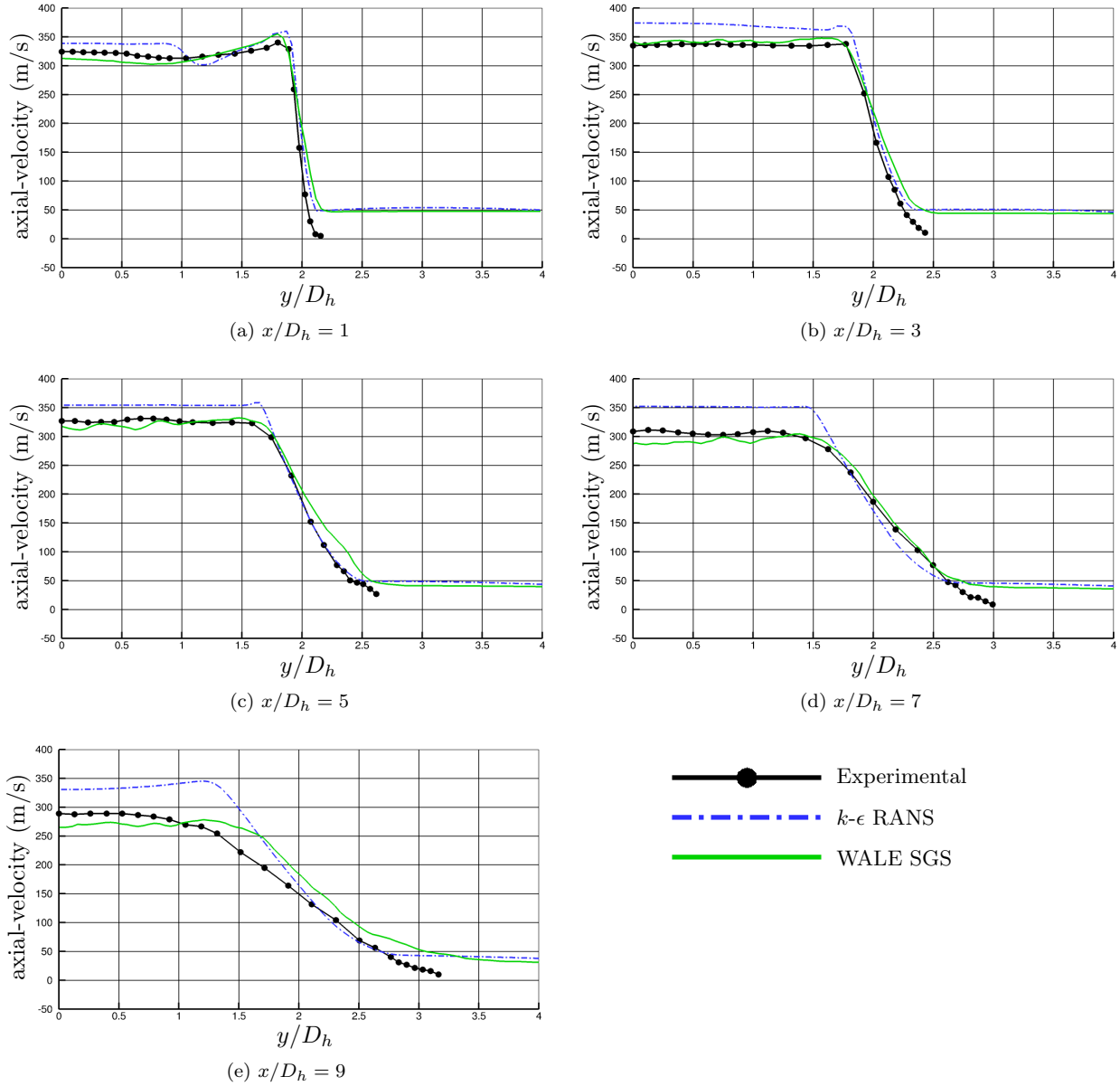Figure 10: Schlieren image and CFD visualisation of the minor axis plane.

(a) $x/D_h = 1$

(b) $x/D_h = 3$

(c) $x/D_h = 5$

(d) $x/D_h = 7$

(e) $x/D_h = 9$

Figure 11: Major axis comparison of axial velocity.

American Institute of Aeronautics and Astronautics

(a) $x/D_h = 1$

(b) $x/D_h = 3$

(c) $x/D_h = 5$

(d) $x/D_h = 7$

(e) $x/D_h = 9$
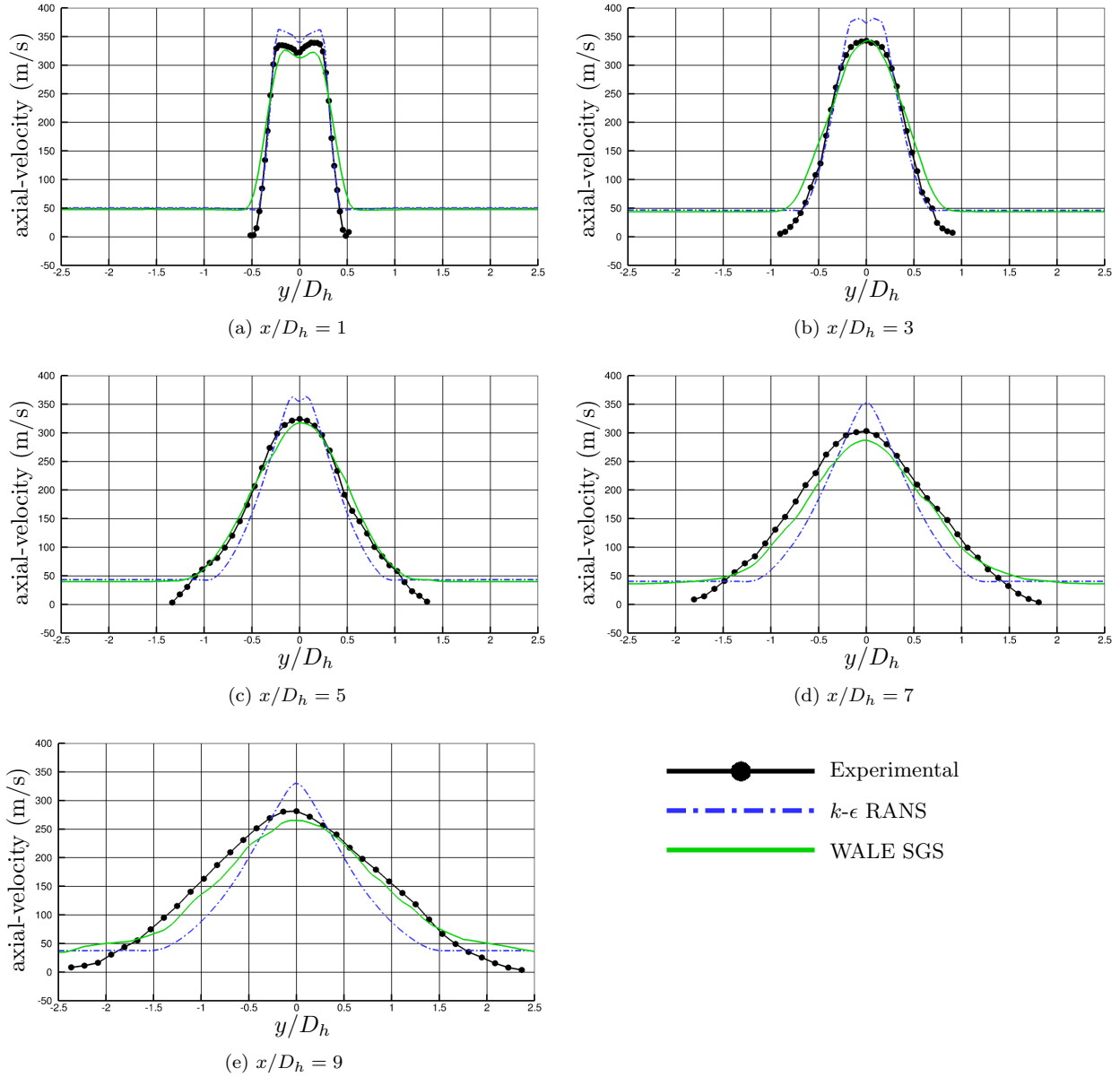
Figure 12: Minor axis comparison of axial velocity.

American Institute of Aeronautics and Astronautics
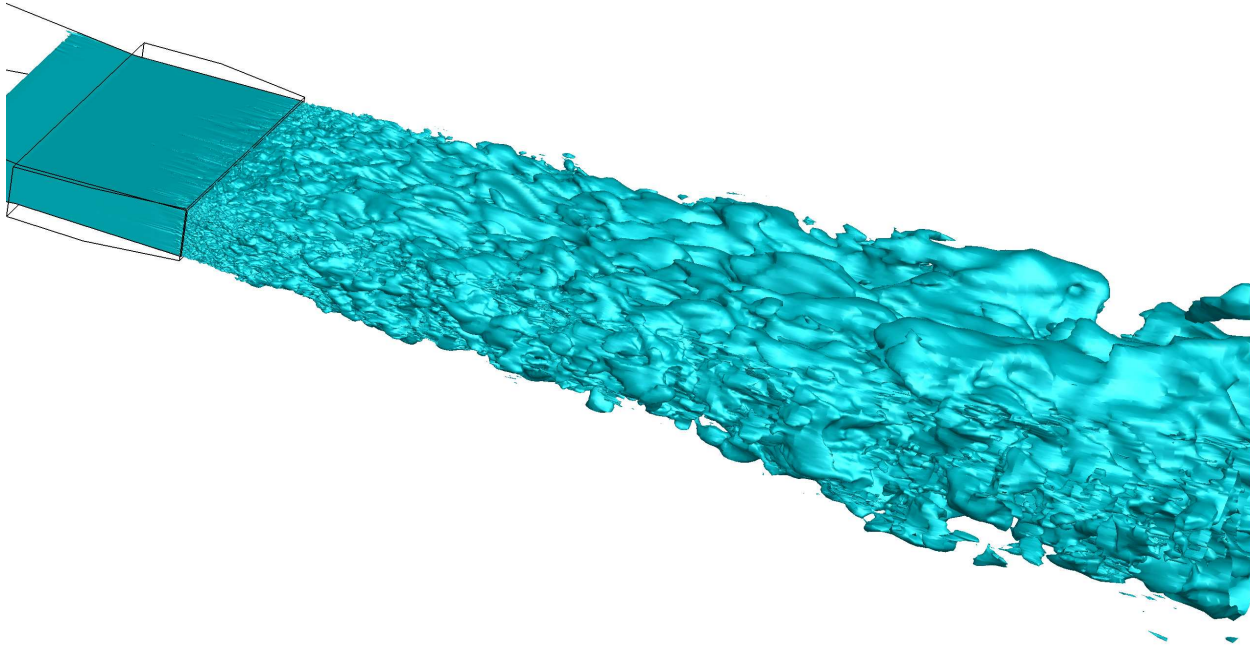
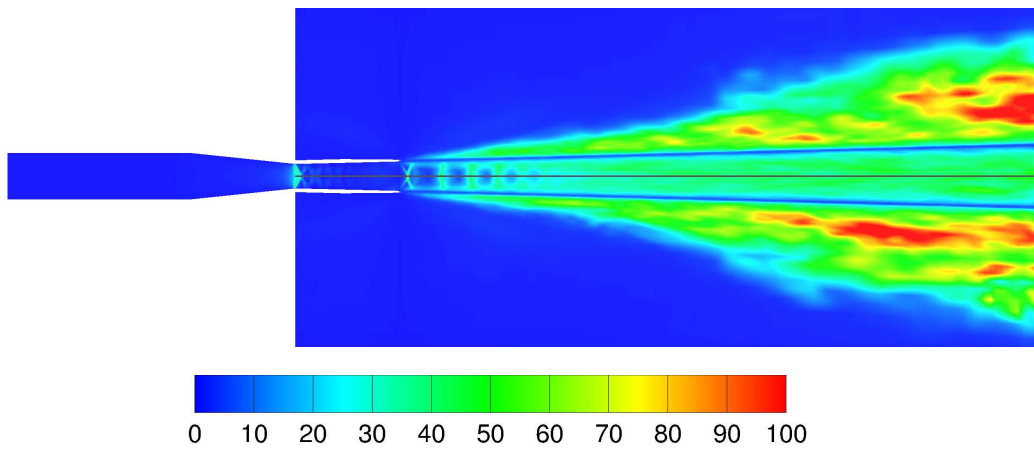Figure 13: Isosurfaces of Mach 0.5 from the WALE simulation.

Figure 14: Mean $\frac{\mu_{\mathrm{SGS}}}{\mu_{\mathrm{Laminar}}}$ ratio flow visualisation across the minor axis plane.

IV. CFD Comparison of Converging S-ducts attached to the RRLU1 Divergent Nozzle

The unconventional aeroengine exhaust system (UAES) combines a contracting S-bend duct with the RRLU1 divergent nozzle. Three different S-duct curvatures (SDC) are considered here: a 53.1° curvature emulating the S-bend of Ng et al., a 70° curvature and a 90° curvature each giving a $1.09D_h$ offset. Along with these three test sections simulations were also ran on a straight contraction section in order to assess the effects of the upstream duct geometry on the flow and to validate the code against the RRLU1 nozzle (seen in section III.B).

IV.A. Geometry

The geometry for the UAES is shown in figure 15. The inlet section is 97.62mm long, with a rectangular cross-section 91.68mm × 25mm, this is followed by one of the four test sections. The first test section, 00° SDC, mirrors the contraction section of the RRLU1 experiment. This is a 67.6mm duct which reduces the height by 47.6% to 13.1mm at the throat. The alternate test sections couple the contraction with an S-bend to offset the inlet from the nozzle exit. The three centreline curvatures are 53.1° (matching the centreline curvature of the Ng[4] S-duct experiment used in the validation study), 70° and 90°. This leads to a $1.09D_h$ offset between the centreline of the inlet and the throat of the nozzle.

The divergent section of the nozzle remains constant through the four separate geometries and comprises of a 55.78mm duct with an increase in duct height of 16.2% to 15.74mm. The final element of the geometry is the coflow domain, starting at the throat and continuing $15D_h$ after the nozzle exit. This has a radius of $4D_h$ at the coflow inlet and a radius of $5D_h$ at the exit.
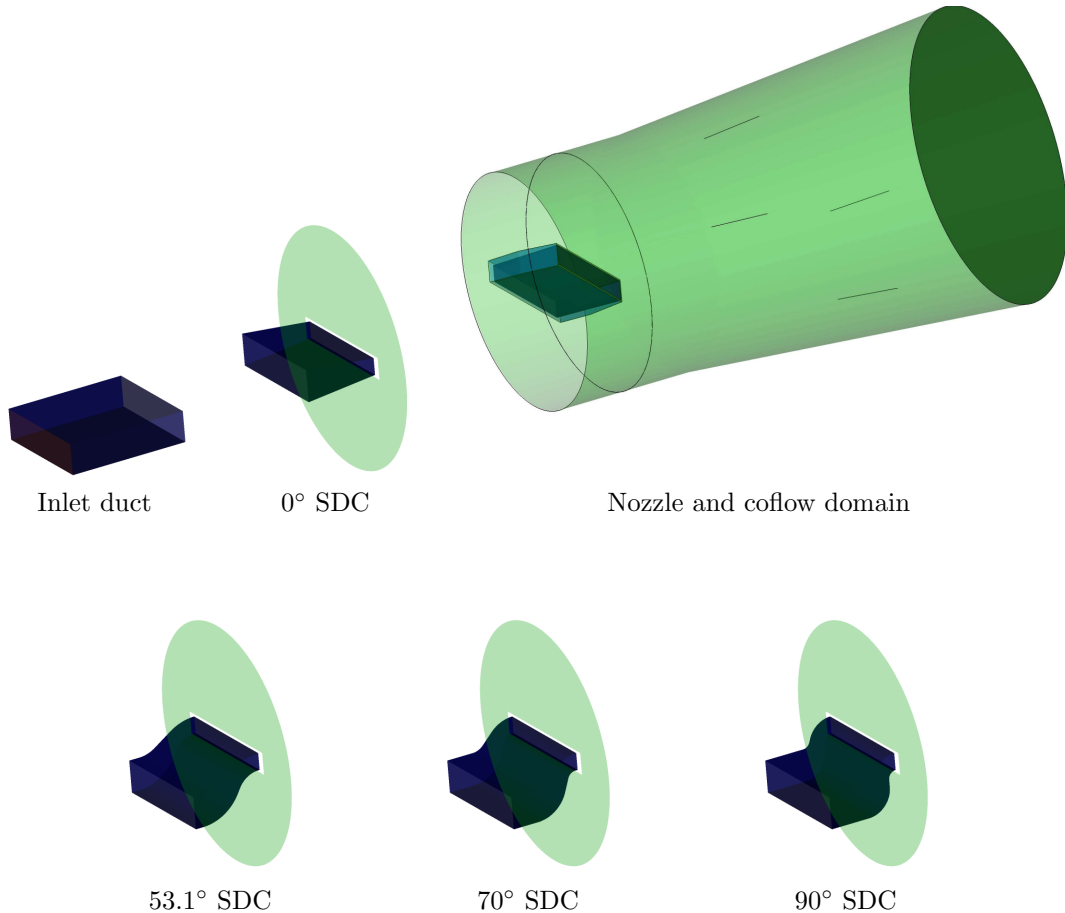

Inlet duct   0° SDC   Nozzle and coflow domain

53.1° SDC   70° SDC   90° SDC

Figure 15: Geometry of the UAES Nozzle Series.

American Institute of Aeronautics and Astronautics

IV.B. Mesh

The UAES uses a hexahedral mesh comprising of approximately $65.5 - 67.5$ million nodes dependent on the test section. The same mesh is used for both RANS simulations and LES. The mesh is significantly finer than is necessary for a RANS calculation however this eliminates any possibly of mesh dependancy influencing the results. The inlet section, as seen in figure 16a, is 153 nodes long with a cross section of 150×220 nodes. This is followed by one of the test sections, figures 16c- 16f, which comprise of a uniform distribution of nodes spaced approximately 0.5mm apart along the major curves. Due to the severity of the curvature, the $90°$ test section includes transition sections between inner and outer curves to allow a more gradual change in streamwise node spacing. The nozzle section contains 220 nodes along the length and can be seen in figure 16b, the Y^+ at the nozzle exit is approximately 1.2. The coflow, figure 16g, is split in to three parts in the streamwise direction. The first section surrounds the nozzle and the second extends $2.5D_h$ downstream of the nozzle requiring 230 nodes. The rest of the coflow is then covered by 150 nodes. The radial component of the coflow contains 40 nodes.
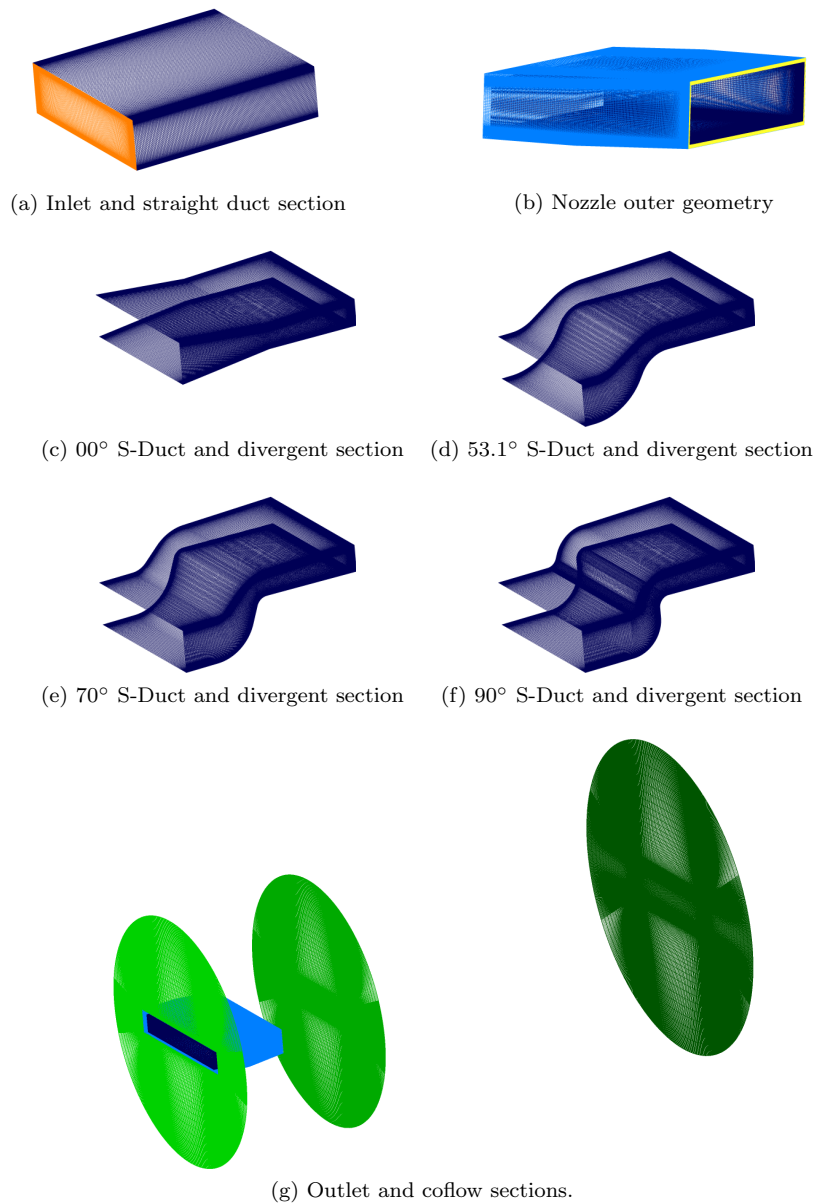

(a) Inlet and straight duct section

(b) Nozzle outer geometry

(c) 00° S-Duct and divergent section

(d) 53.1° S-Duct and divergent section

(e) 70° S-Duct and divergent section

(f) 90° S-Duct and divergent section

(g) Outlet and coflow sections.

Figure 16: Mesh of the UAES series nozzles.

American Institute of Aeronautics and Astronautics

IV.C.   RANS modelling of the UAES

Initial predictions of the three UAES geometries were conducted using the k-ϵ RANS model. Figure 17 shows the axial-velocity at the minor axis plane. Although there is little difference in the 53.1° case there is a clear trend seen in the greater curvatures. Both 70° and 90° S-bend geometries see a shortening potential core length as well as a deflection in the aerodynamic centreline of the potential core which is raised above the geometric centreline of the nozzle by approximately 2°. The latter may be due to the increased mixing in the underside of the jet caused by a pressure imbalance at the nozzle.

The effective NPR at the nozzle exit, reduction in mass flow rate and thrust loss were measured at the nozzle exit plane. All three S-duct curvatures suffered a loss in the three metrics with greater losses occurring with increased curvature, as shown in table 1.

Due to the upward deflection of the potential core in the 70° and 90° cases the geometric centreline velocities would not be appropriate for a comparison of the flow. Consequently measurements are taken along the aerodynamic centre of the plume in order to compare velocities (shown in figure 18). Here we confirm that the potential core length is reduced as the curvature of the S-bend duct section increases.
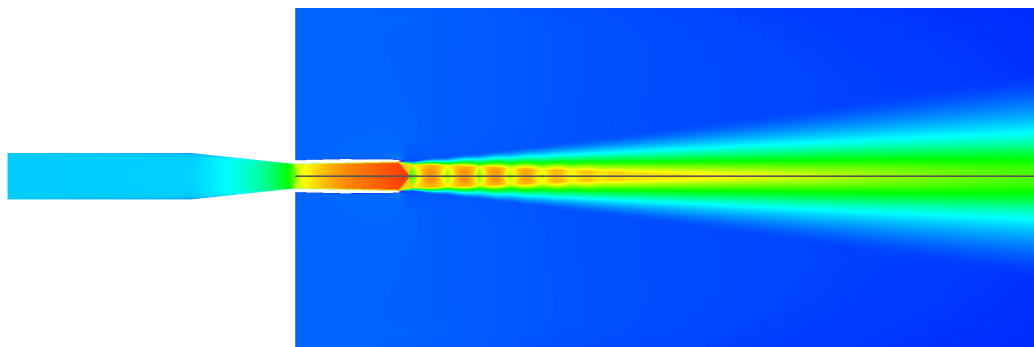
The effect of the upstream duct curvature on the shock cells is seen in figure 19. Here we see, as expected, a decrease in the number of shock cells as well as a reduction in the length of the individual cell. This reduction will be due to the pressure loss, and consequently the change in effective NPR at the nozzle exit, caused by the upstream duct curvature. The images seen in figure 19 also include the divergent nozzle in comparison to those shown earlier in figure 10. The imbalances within the fluid profile caused by the S-bend also cause the shock structures to alter within the divergent section of the nozzle.

In figure 20 we see a series of cut planes along the length of the domain showing the total pressure coefficient based on inlet total and ambient static pressure. At the exit plane of the S-duct a transverse total pressure gradient exists for all three curvatures. Along the upper edge of the S-duct exit plane there is a band of high pressure, this then decrease towards the lower edge. The lowest 20% of the duct then sees a sharp rise in total pressure again. This transverse total pressure gradient influences the development of the flow causing the plume to move and change shape. Looking at the 70° case, the transverse total pressure gradient seen at the S-duct exit plane is sustained as the jet plume develops. The total pressure deficit below the geometric centreline, and subsequent lower velocity region, causes the peak velocity to be above the geometric centreline. This gives the impression of the deflection of the plume away from the geometric centreline.
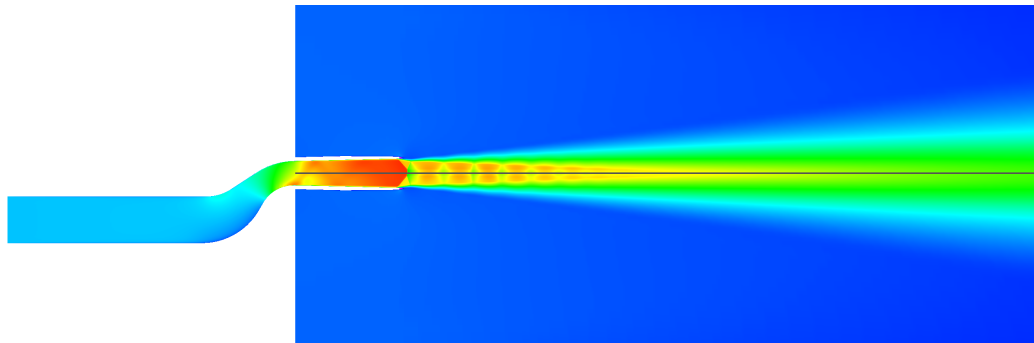
The tapering at the minor edges of the plume is seen in all cases however this is impacted upon in both the 70° and 90° S-duct curvatures by the transverse total pressure gradient of the S-duct exit plane. The upper half of the plume is sustained longer than the lower due to the high total pressure region along the upper half of the plume which leads to the trapezoidal shape seen in the downstream planes of the 70° and 90° cases in figure 20. This in turn leads to a more circular shaped jet plume $15D_h$ down stream of the nozzle exit.

S-duct Curvature	Effective NPR	Reduction in Mass Flow Rate	Thrust Loss
0°	2.35	0%	0%
53.1°	2.31	3.57%	3.57%
70°	2.21	9.65%	9.21%
90°	2.09	12.31%	17.51%

Table 1: Numerical effects of altering the SDC on the flow at the nozzle exit plane for RANS modelling.
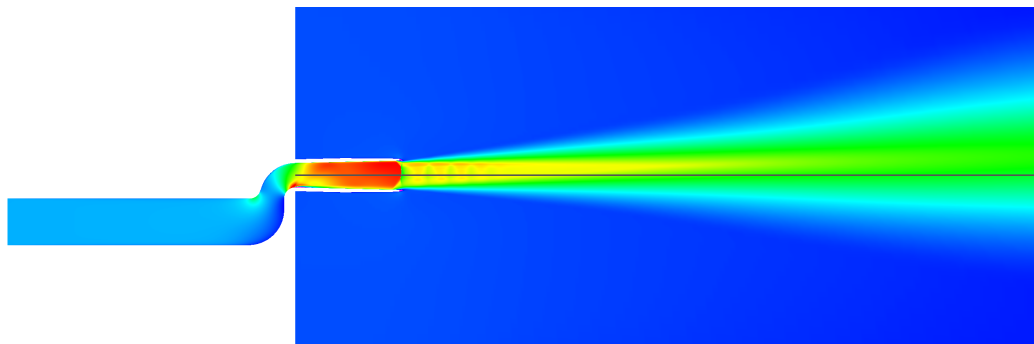
American Institute of Aeronautics and Astronautics

(a) 0° S-Duct Curvature

(b) 53.1° S-Duct Curvature

(c) 70° S-Duct Curvature

(d) 90° S-Duct Curvature

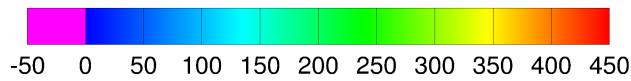-50   0   50   100   150   200   250   300   350   400   450
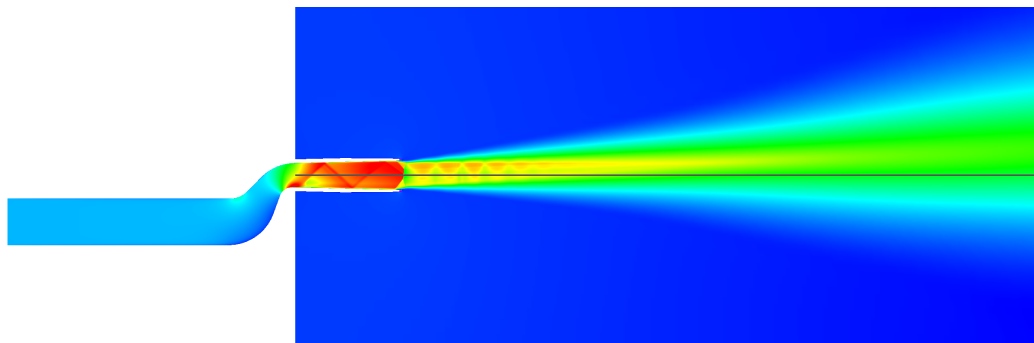
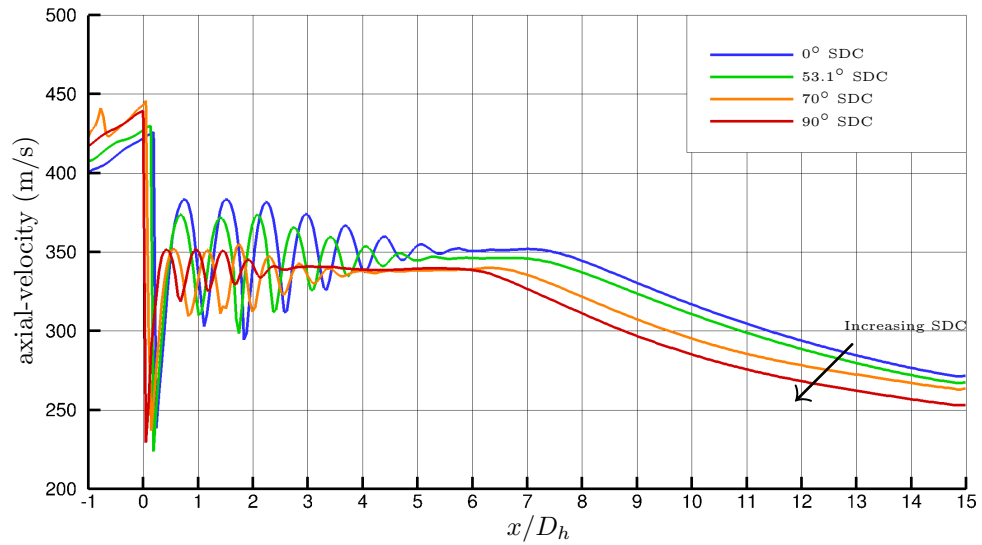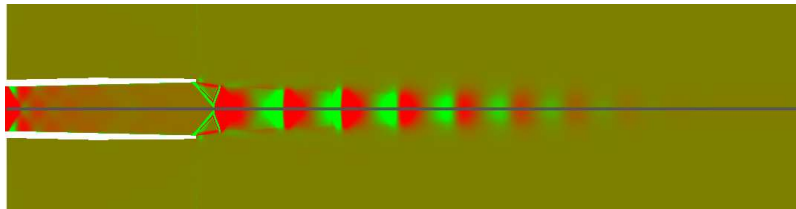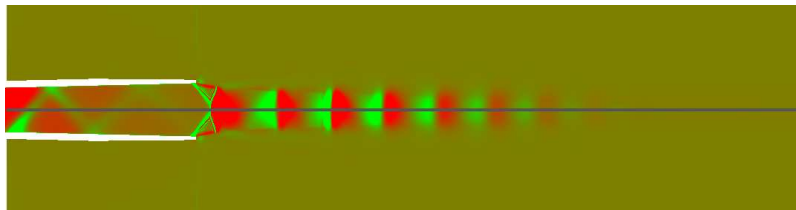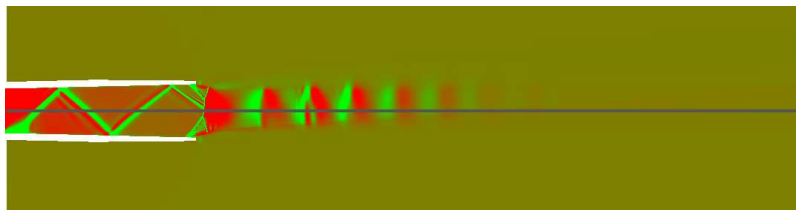Figure 17: RANS flow visualisation of axial velocity across the minor axis plane.

Figure 18: Axial-velocity comparison along the aerodynamic centre of the plume using the k-ϵ turbulence model.
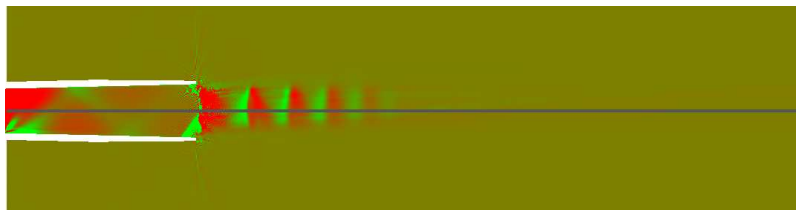

(a) 0° S-Duct Curvature

(b) 53.1° S-Duct Curvature

(c) 70° S-Duct Curvature

(d) 90° S-Duct Curvature

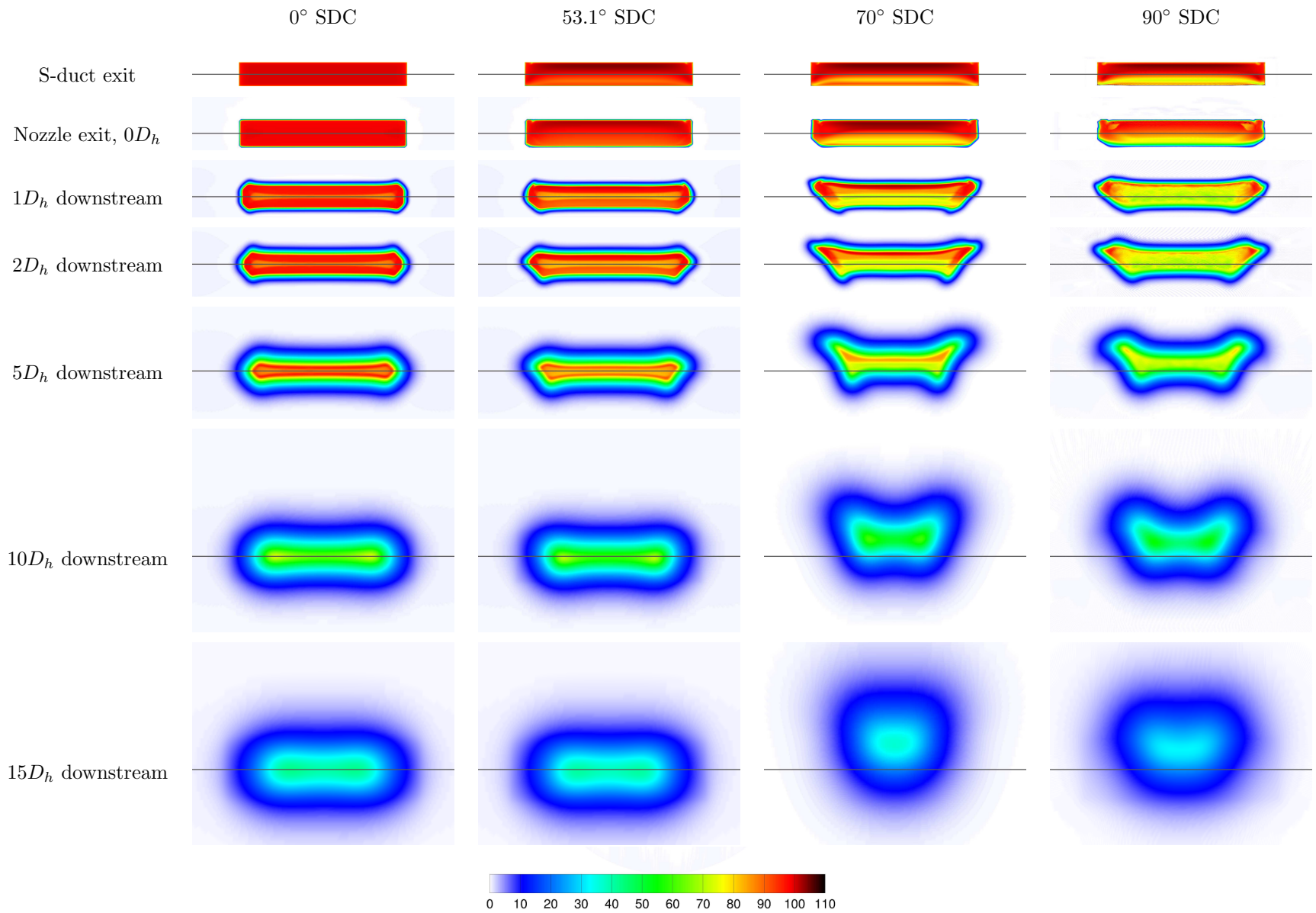Figure 19: RANS schlieren image and CFD visualisation of the minor axis plane.

Figure 20: RANS cross section flow visualisations of total pressure coefficient.

IV.D.   LES modelling of the UAES

Similar to what was seen in subsection IV.C, the LES predictions show a reduction in the potential core length. This can be seen in the axial velocity profiles taken on the minor axis plane of the three cases, figure 21. The centre of the potential core in the LES simulations is deflected in the opposite direction to the RANS predictions by about the same magnitude for the 70° and 90° S-duct curvature cases. This deflection towards the S-bend is likely to again be a reflection of the transverse pressure gradients found in the nozzle exit plane.

The metrics discussed in the RANS modelling: effective NPR, reduction in mass flow rate and thrust loss, are given for the LES cases in table 2. There are a few differences between the LES and RANS simulations. The effective NPR is slightly higher for the LES cases and for both the 70° and 90° S-duct curvatures the reduction in mass flow rates are again slightly greater in comparison to the RANS simulations. The most notable difference, however, is the reduction in thrust loss seen in the 53.1° S-duct curvature LES case where an improvement of over 50% can be seen in comparison to the RANS simulation.

Figure 22 compares the velocity along the aerodynamic centre of the plume between the RANS and large eddy simulations for the three S-duct curvatures (as stated in subsection IV.C, due to the deflection of the potential core in the RANS simulations the centre of the plume is used for the comparison data). In all three S-duct curvatures we see a similar reduction in the potential core length as well as a shift in the shock cell location that was also seen in the equivalent comparison in the validation study (subsection III.B, figure 7). With the LES cases we also see the same relationship between the potential core length and S-duct curvature that was seen with the RANS (figure 23). Similar effects on the shock cell location are also seen in the LES cases, however, the drop in velocity for greater S-duct curvatures is not seen to the same extent as in the RANS cases.

It should be noted here that there were some issues in keeping the 70° S-duct curvature simulation stable for the LES calculations. It would be beneficial for the mesh to receive the same treatment as the the 90° S-duct curvature mesh did in future work, namely adapting the S-bend section to include transition sections of mesh between inner and outer curves in order to give a more gradual change to the node spacing. Due to this instability 30% fewer samples were obtained for the mean of the 70° case, too few to provide a statistically meaningful average beyond the potential core region (around $4D_h$ downstream of the nozzle exit).
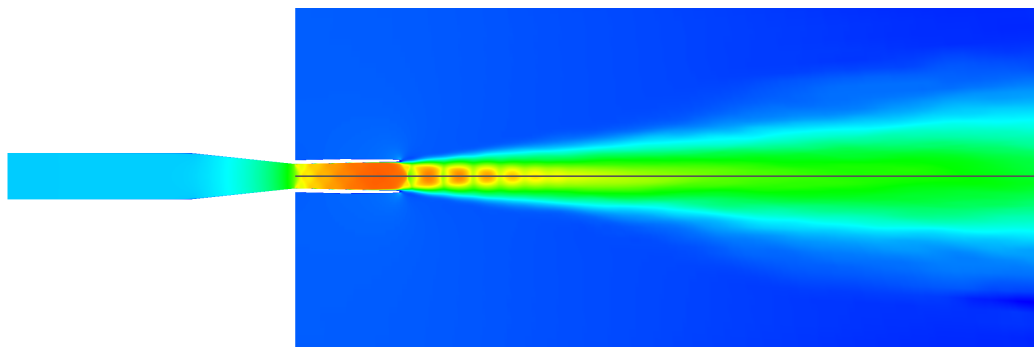
The axial density gradient visualisations using LES, figure 24 also show similar trends to those of the RANS simulations. Fewer shock cells are seen with increasing S-duct curvature as well as a shift in location corresponding to the drop in effective nozzle NPR. The changes in the nozzle shock structure is also seen in the LES visualisations.

In figure 25 we again see a series of cut planes along the length of the domain similar to those shown in figure 20. Although the evolution of the profiles for the validation, 0° SDC, case match reasonably well against the RANS predictions seen earlier (allowing for the effects of a shorter potential core) there are significant differences between the solutions of the two CFD methods. The most obvious difference lies in the shape of the potential core for all cases. In the validation case the tapering of the potential core at the minor edges is not seen to the same extent which results in the rectangular shape being sustained until after the end of the potential core. This, coupled with the substantial change in the transverse total pressure gradient of the S-duct exit plane, leads to a less drastic change in plume shape as the S-duct curvature increases.
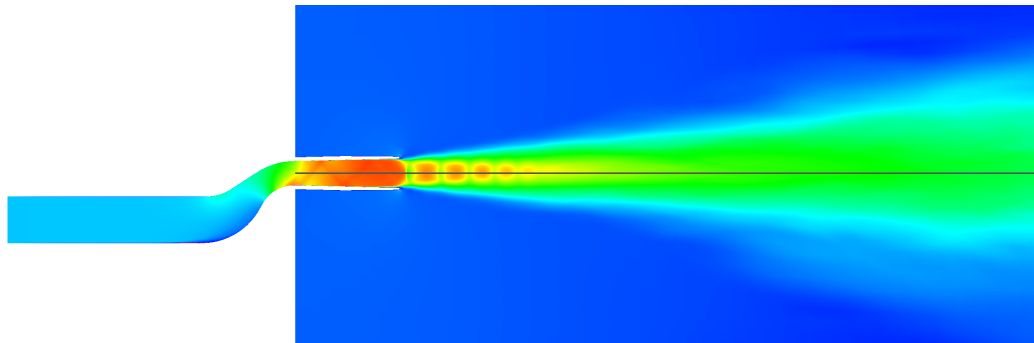
At the three different S-duct exit planes the transverse total pressure gradient as seen in the RANS simulations is not apparent. Only the high pressure region at the lower edge of the duct still exists which gives rise to the apparent deflection of the potential core in this direction.

S-duct Curvature	Effective NPR	Reduction in Mass Flow Rate	Thrust Loss
0°	2.36	0%	0%
53.1°	2.34	2.82%	1.59%
70°	2.18	10.01%	9.83%
90°	2.14	13.92%	16.15%

Table 2: Numerical effects of altering the SDC on the flow at the nozzle exit plane for LES modelling.

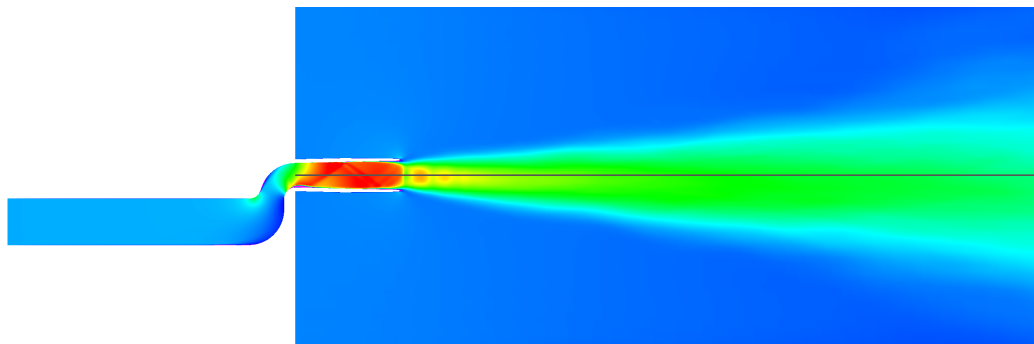American Institute of Aeronautics and Astronautics

(a) 0° S-Duct Curvature

(b) 53.1° S-Duct Curvature

(c) 70° S-Duct Curvature

(d) 90° S-Duct Curvature

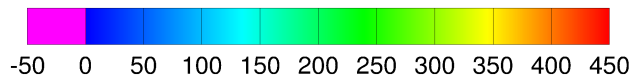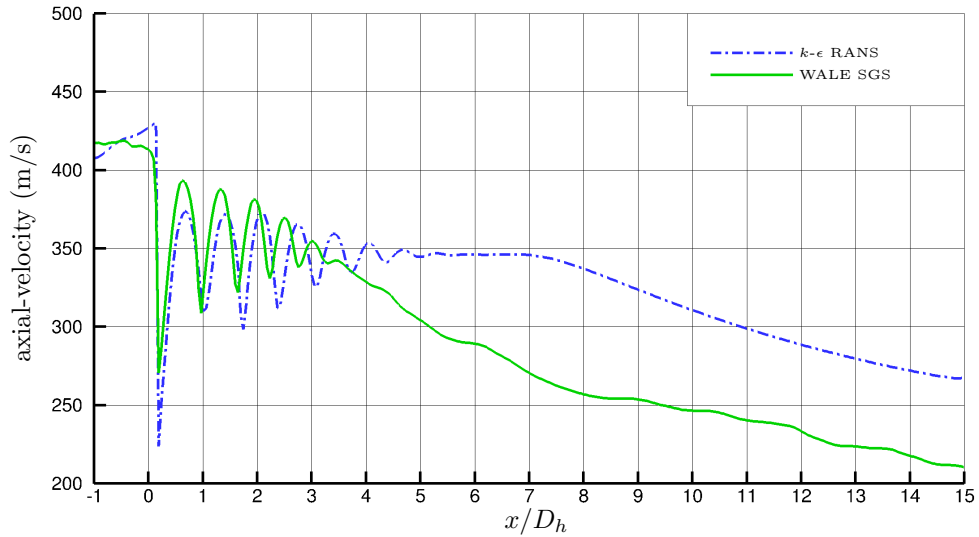-50   0   50   100 150 200 250 300 350 400 450
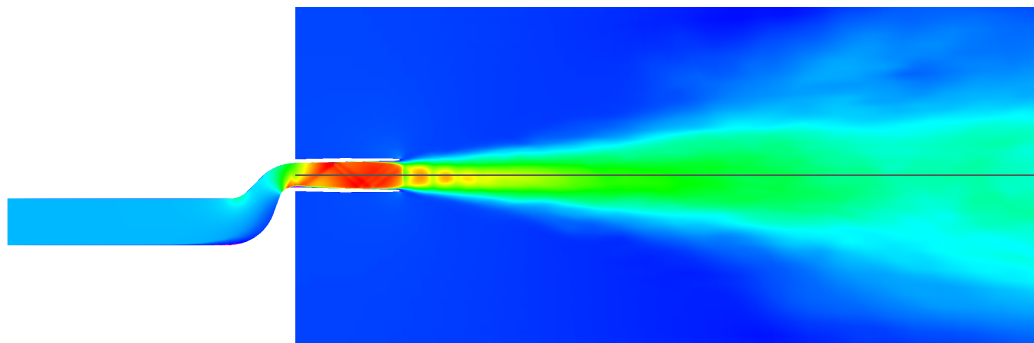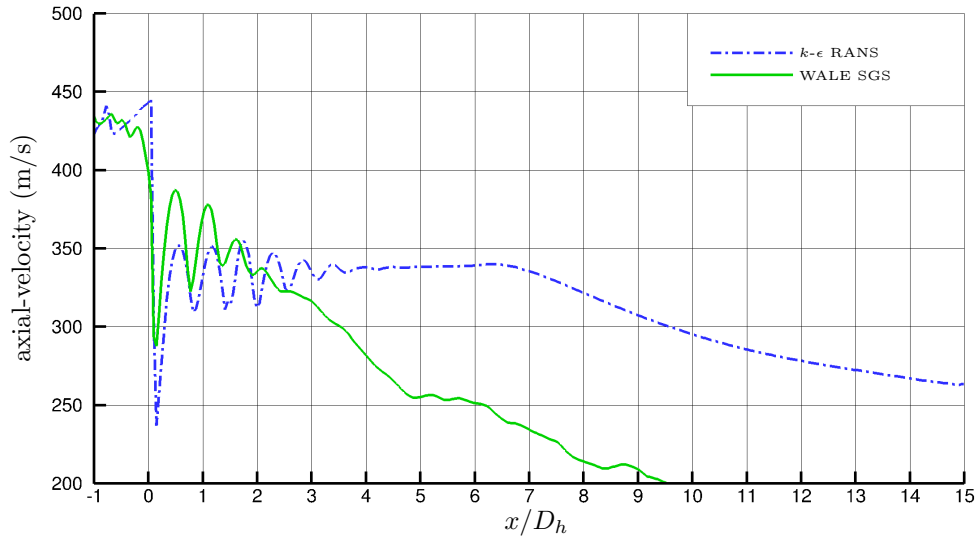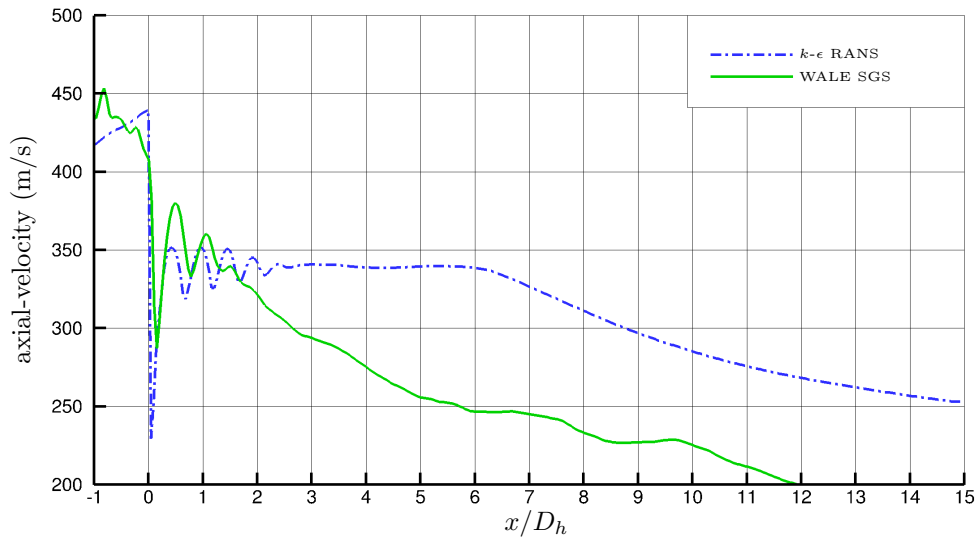
Figure 21: LES flow visualisation of axial velocity across the minor axis plane.

(a) 53.1° S-Duct Curvature

(b) 70° S-Duct Curvature

(c) 90° S-Duct Curvature

Figure 22: Axial-velocity comparison along the aerodynamic centre of the plume between RANS and LES.
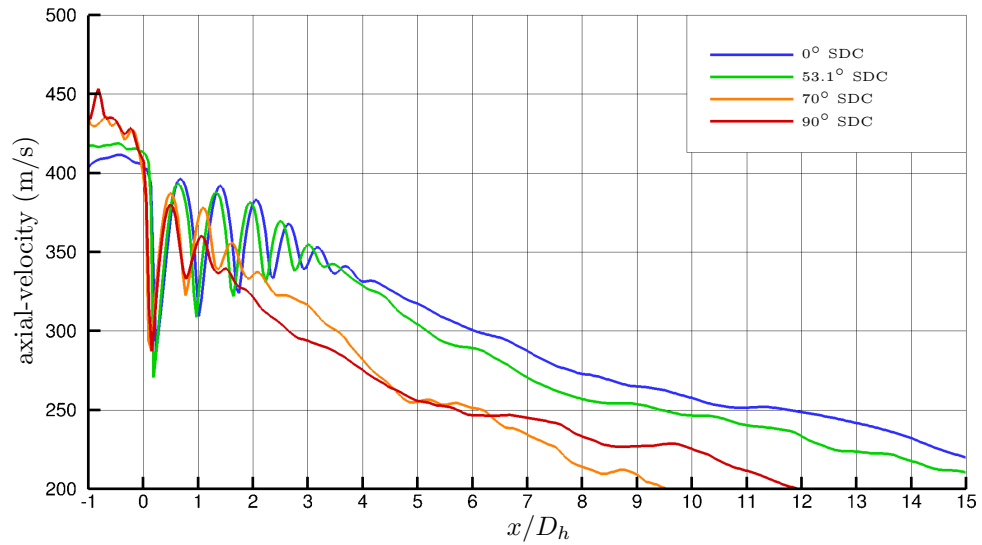
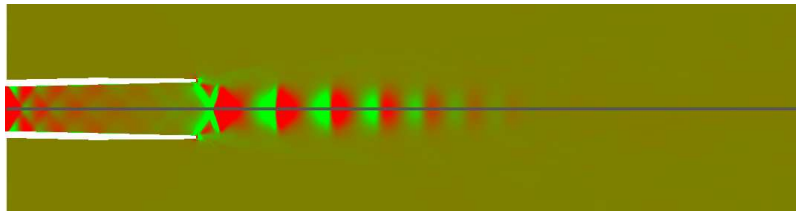American Institute of Aeronautics and Astronautics
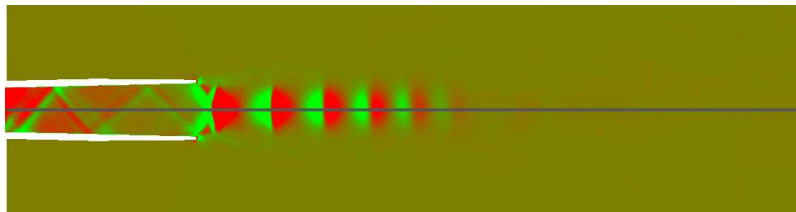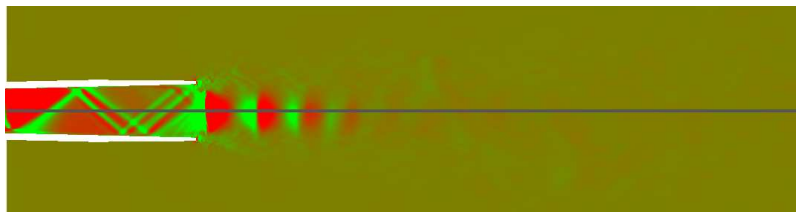
Figure 23: Axial-velocity comparison along the aerodynamic centre of the plume using the WALE SGS model.
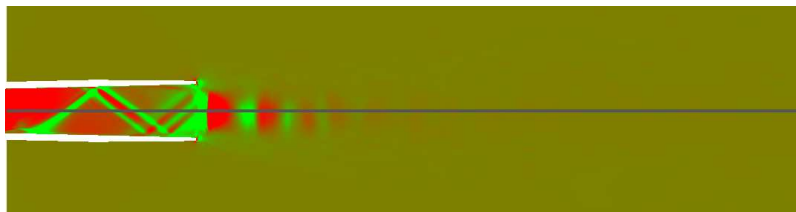

(a) 0° S-Duct Curvature

(b) 53.1° S-Duct Curvature

(c) 70° S-Duct Curvature

(d) 90° S-Duct Curvature

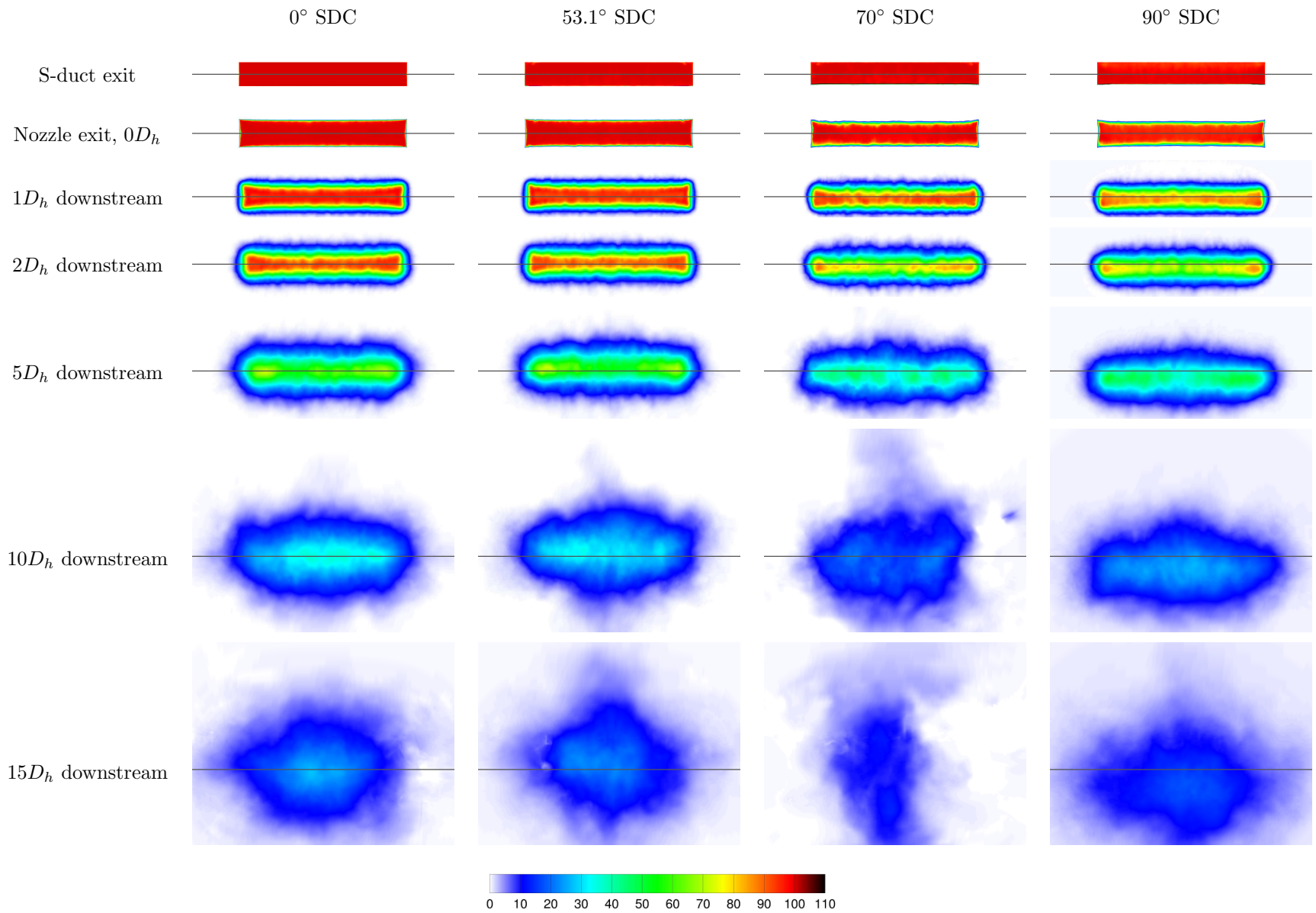Figure 24: LES schlieren image and CFD visualisation of the minor axis plane.

Figure 25: LES cross section flow visualisations of total pressure coefficient.

V.   Conclusion

The results of validation of the rectangular nozzle, subsection III.B, show that there is a significant benefit in the use of LES for modelling high speed jets from high aspect ratio nozzles. In comparison with a k-ϵ RANS simulation the LES shows a $3D_h$ reduction in potential core length which almost matches the experimental data. Likewise the centreline peaks and shear layer gradients of the experimental major and minor axis axial velocity profiles are matched by the LES predictions at several axial stations downstream of the nozzle exit. In comparison, the RANS simulation both over predicts the peak velocity at all axial stations and has a steeper gradient for the shear layer.

The effect of convoluting the upstream convergence section of the RRLU1 nozzle was shown in section IV. All three S-duct convolutions showed a reduction in the potential core length of the jet for the RANS simulations ranging from a 3.7% reduction for an S-duct curvature of 53.1° to a 20.5% reduction for an S-duct curvature of 90°. This was also the case for the LES predictions, however, the reductions in potential core length were greater, ranging from a 16% reduction for the 53.1° S-duct curvature to around a 50% reduction for the 90° S-duct curvature. A reduction in the effective NPR at the nozzle exit due to duct losses was seen along with a reduction in both the mass flow rate and thrust for all three curvatures, increasing with the severity of the S-duct curvature.

The RANS predictions of the three variations of upstream duct also display the existence of a transverse total pressure gradient across the exit plane of the nozzle. As the S-duct curvature increases, the shape of the jet plume also changes from rectangular to trapezoidal with the longest edge aligned with the upper surface of the nozzle. This is due to a combination of the transverse total pressure gradient and the tapering already seen along the minor edges of the jet plume in the RANS validation, 0° SDC, case. The aerodynamic centreline of the jet plume issuing from the nozzle moves away from the geometric centreline with an increasing deflection as the S-duct curvature increases.

The transverse total pressure gradient is also seen in the LES predictions however it lacks the higher total pressure region located along the upper edge of the S-duct exit plane. This change in the total pressure profile at the S-duct exit plane impacts on the deflection of the potential core for the LES cases. The aerodynamic centreline of the plume is now deflected in the opposite direction to the RANS simulations, below the geometric centreline, but to a similar magnitude. The shape of the jet plume in the LES predictions is also affected by the change in transverse pressure gradient and remains closer to the original rectangular shaped plume of the LES validation, 0° SDC, case.

The upstream S-bend has a significant effect on the high speed, high aspect ratio jet development leading to improved mixing and shorter potential core length for a given imposed pressure ratio. However, this improvement comes at a reduction in mass flow rate and consequent thrust loss. These trends are seen in all three duct curvatures, for both RANS and LES predictions, and must be taken into account when designing future unconventional aeroengine exhaust systems.

Acknowledgments

References

[1]Miller, D. S., *Internal Flow Systems*.

[2]Prandtl, L., *Prandtl's Essentials of Fluid Mechanics*, Springer, 2nd ed., 1953.

[3]Bansod, P. and Bradshaw, P., "The Flow in S-shaped Ducts," *Aeronautical Quarterly*, Vol. 23, May 1972, pp. 131–140.

[4]Ng, Y. T., Luo, S. C., Lim, T. T., and Ho, Q. W., "On swirl development in a square cross-sectioned S-shaped duct," *Experiments in Fluids*, Vol. 41, 2006, pp. 975–989.

[5]Taylor, A. M. K. P., Whitelaw, J. H., and Yianneskis, M., "Developing Flow in S-Shaped Ducts I: Square Cross-Section Duct," NASA Contractor Report 3550, May 1982.

[6]Vakili, A., Wu, J. M., Liver, P., and Bhat, M. K., "An Experimental Investigation of Secondary Flows in a S-Shaped Duct," Nasa lewis final report, 1983.

[7]Vakili, A., Wu, J. M., Bhat, M. K., and Liver, P., "Compressible Flow in a Diffusing S-Duct with Flow Separation," *Heat Transfer and Fluid Flow in Rotating Machinery*, edited by W. J. Yang, Hemisphere Publishing, 1987, pp. 201–211.

[8]Vakili, A., Wu, J. M., Liver, P., and Bhat, M. K., "Measurements of Compressible Secondary Flow in a Circular S-Duct," AIAA Paper 83-1739, July 1983.

[9]Vakili, A., Wu, J. M., Hingst, W. R., and Towne, C. E., "Comparison of Experimental and Computational Compressible Flow in a S-Duct," AIAA Paper 84-0033, January 1984.

[10]Smith, C. F., Bruns, J. E., Harloff, G. J., and DeBonis, J. R., "Three Dimensional Compressible Turbulent Computations for a Non Diffusing S-Duct," NASA Contractor Report 4391, April 1991.

[11]Smith, C. F., Bruns, J. E., Harloff, G. J., and DeBonis, J. R., "Three Dimensional Compressible Turbulent Computations for a Diffusing S-Duct," NASA Contractor Report 4392, April 1992.

[12]Guo, R. W. and Seddon, J., "The Swirl in an S-Duct of Typical Intake Proportions," *Aeronautical Quarterly*, Vol. 34, May 1983, pp. 99–129.

[13]Guo, R. W. and Seddon, J., "Swirl Characteristics of an S-Shaped Air Intake with both Horizontal and Vertical Offsets," *Aeronautical Quarterly*, Vol. 34, May 1983, pp. 130–146.

[14]Sforza, P. M., Steiger, M. H., and Trentacoste, N., "Studies on Three-Dimensional Viscous Jets," *AIAA Journal*, Vol. 4, No. 5, May 1966, pp. 800–806.

[15]Trentacoste, N. and Sforza, P., "Further Experimental Results for Three-Dimensional Free Jets," *AIAA Journal*, Vol. 5, No. 5, May 1967, pp. 885–891.

[16]Sforza, P. M., "A Quasi-Axisymmetric Approximation for Turbulent, Three-Dimensional Jets and Wakes," *AIAA Journal*, Vol. 7, No. 7, 1969, pp. 1380–1383.

[17]Sfeir, A. A., "The Velocity and Temperature Fields of Rectangular Jets," *International Journal of Heat and Mass Transfer*, Vol. 19, 1976, pp. 1289–1297.

[18]Tsuchiya, Y., Horikoshi, C., and Sato, T., "On the Spread of Rectangular Jets," *Experiments in Fluids*, Vol. 4, 1986, pp. 197–204.

[19]Mi, J., Nathan, G. J., and Luxton, R. E., "Centreline Mixing Characteristics of Jets From Nine Differently Shaped Nozzles," *Experiments in Fluids*, Vol. 28, 2000, pp. 93–94.

[20]Mi, J. and Nathan, G. J., "Statistical Properties of Turbulent Free Jets Issuing from Nine Differently-Shaped Nozzles," *Flow, Turbulence and Combustion*, 2009.

[21]Gutmark, E. J. and Grinstein, F. F., "Flow Control with Noncircular Jets," *Annual Review of Fluid Mechanics*, Vol. 31, 1999, pp. 239–272.

[22]Miller, R. S., Madnia, C. K., and Givi, P., "Numerical Simulation of Non-Circular Jets," *Computers and Fluids*, Vol. 24, No. 1, 1995, pp. 1–25.

[23]Mendez, S., Shoeybi, M., Sharma, A., Ham, F. E., Lele, S. K., and Moin, P., "Large-Eddy Simulations of Perfectly Expanded Supersonic Jets Using an Unstructured Solver," *AIAA Journal*, Vol. 50, No. 5, May 2012, pp. 1103–1118.

[24]Nichols, J. W., Ham, F. E., and Lele, S. K., "High-Fidelity Large-Eddy Simulation for Supersonic Rectangular Noise Prediction," *Proceedings of 17th AIAA/CEAS Aeroacoustics Conference*, 2011.

[25]Crumpton, P. I., Moinier, P., and Giles, M. G., "An Unstructured Algorithm for High Reynolds Number Flows on Highly Stretched Grids," *10th International Conference on Numerical Methods for Laminar and Turbulent Flow*, 1998.

[26]Page, G. J. and McGuirk, J. J., "Large Eddy Simulation of a Complete Harrier Aircraft in Ground Effect," *Aeronautical Journal*, Vol. 113, No. 1140, 2009, pp. 99–106.

[27]Moinier, P. I., *Algorithm Developments for an Unstructured Viscous Flow Solver*, Ph.D. thesis, University of Oxford, Oxford, UK, 2009.

[28]Menter, F. R., "Zonal Two Equation k- Turbulence Models for Aerodynamic Flows," AIAA Paper 93-2906, 1993.

[29]Menter, F. R., "Two-Equation Eddy-Viscosity Turbulence Models for Engineering Applications," *AIAA Journal*, Vol. 32, 1994, pp. 1598–1605.

[30]Nicoud, F. and Ducros, F., "Subgrid-Scale Stress Modelling Based on the Square of the Velocity Gradient Tensor," *Flow, Turbulence and Combustion*, Vol. 62, 1999, pp. 183–200.

[31]Vuillerme, A. L., Deck, S., and Chevrier, R., "Numerical Simulations of the Flow Inside an S-Shaped Intake Diffuser," *Proceedings of European Conference for Aerospace Sciences*, 2006.

[32]Behrouzi, P. and McGuirk, J. J., "Modelling of Civil and Military Exhaust Systems - High Speed Jet Plume Experimental Study - Phase-2 Part-1 - RRLU-1 Nozzle - Full Experimental Results," Tech. rep.

[33]Behrouzi, P. and McGuirk, J. J., "Modelling of Civil and Military Exhaust Systems - High Speed Jet Plume Experimental/CFD Study - Phase-2 Part-3 - Effect of Nozzle Exit Shape on Jet Flow Development (RRLU-7 and RRLU-8 Nozzles)," Tech. rep.